Beyond the Pixel: Using Patterns and Multiscale Spatial Information to Improve the Retrieval of Precipitation from Spaceborne Passive Microwave Imagers

CLÉMENT GUILLOTEAU

Department of Civil and Environmental Engineering, University of California, Irvine, Irvine, California

EFI FOUFOULA-GEORGIOU

Department of Civil and Environmental Engineering, and Department of Earth System Science, University of California, Irvine, Irvine, California

(Manuscript received 15 April 2019, in final form 22 November 2019)

ABSTRACT

The quantitative estimation of precipitation from orbiting passive microwave imagers has been performed for more than 30 years. The development of retrieval methods consists of establishing physical or statistical relationships between the brightness temperatures (TBs) measured at frequencies between 5 and 200 GHz and precipitation. Until now, these relationships have essentially been established at the ''pixel'' level, associating the average precipitation rate inside a predefined area (the pixel) to the collocated multispectral radiometric measurement. This approach considers each pixel as an independent realization of a process and ignores the fact that precipitation is a dynamic variable with rich multiscale spatial and temporal organization. Here we propose to look beyond the pixel values of the TBs and show that useful information for precipitation retrieval can be derived from the variations of the observed TBs in a spatial neighborhood around the pixel of interest. We also show that considering neighboring information allows us to better handle the complex observation geometry of conical-scanning microwave imagers, involving frequency-dependent beamwidths, overlapping fields of view, and large Earth incidence angles. Using spatial convolution filters, we compute ''nonlocal'' radiometric parameters sensitive to spatial patterns and scale-dependent structures of the TB fields, which are the ''geometric signatures'' of specific precipitation structures such as convective cells. We demonstrate that using nonlocal radiometric parameters to enrich the spectral information associated to each pixel allows for reduced retrieval uncertainty (reduction of 6%–11% of the mean absolute retrieval error) in a simple *k*-nearest neighbors retrieval scheme.

1. Introduction

Since the first experimental algorithms developed for the SMMR (see appendix A for all acronyms used in this article) imager in the 1980s, the algorithms performing the retrieval of precipitation from passive microwave imagers in orbit have been continuously evolving and improving (Wilheit and Chang 1980; Spencer 1986; Spencer et al. 1989; Wilheit et al. 1991; Liu and Curry 1992; Kummerow and Giglio 1994; Petty 1994; Ferraro and Marks 1995; Kummerow et al. 1996, 2001, 2015; Kubota et al. 2007; Gopalan et al. 2010; Mugnai et al. 2013; Ebtehaj et al. 2015; Kidd et al. 2016; Petković et al. 2018). The TRMM (Kummerow et al. 2000) and GPM (Hou et al. 2014; Skofronick-Jackson et al. 2017) satellite missions in particular provided the data and the research framework allowing the successful development of research and operational retrieval algorithms. Today, the GPM Microwave Imager (GMI) is integrated in an international constellation of orbiting imagers providing frequent observations of clouds and precipitation all over the globe (Skofronick-Jackson et al. 2018).

The passive microwave retrieval of precipitation relies on the measurement of radiances at the top of the atmosphere, which are the product of the surface emission, emission and absorption by liquid rain drops and water vapor and scattering by ice particles. Vertically and

Denotes content that is immediately available upon publication as open access.

Corresponding author: Clément Guilloteau, cguillot@uci.edu

DOI: 10.1175/JTECH-D-19-0067.1

horizontally polarized radiances are measured at various frequencies between 5 and 200 GHz and converted into brightness temperatures (TBs) for physical interpretation. The physical principles of the radiative transfer of microwaves in the atmosphere are well understood and generally accurately reproduced by numerical models. However, the conversion of observed microwave multispectral signatures into hydrometeor profiles (inverse problem) remains uncertain. This uncertainty derives mostly from the inherent underdetermined nature of the inverse problem, that is, while any given hydrometeor profile has a unique spectral signature (assuming known surface emissivity) the inverse is not true (Bauer et al. 2001; Löhnert et al. 2001; Sanò et al. 2013; Ebtehaj et al. 2015). The increasing number of available channels (up to 13 and 14 channels respectively for GMI and AMSR-2, which are the most recent radiometers sent into orbit) allows a better constraining of the inversion, but nonnegligible uncertainty still affects the state-of-the-art retrievals.

Many algorithms, among which the NASA operational algorithm GPROF (Kummerow et al. 2015), rely on an a priori database (or dictionary) for the retrieval. The a priori database is made of a large number of hydrometeor profiles, each one associated with a spectral signature, that is, a vector of TBs. The database is typically obtained from actual radiometric measurements collocated with radar observations, or generated using a radiative transfer model to simulate brightness temperatures from the radar-observed hydrometeor profiles. The retrieval generally relies on the computation of radiometric distances (vectorial distances) between the observed TB vector and the TB vectors of the a priori database to find one or several hydrometeor profiles with a spectral signature close to the observation (called the ''neighbors''). An important element in the development of distance-based retrieval algorithms is the choice of the distance metric (Hastie et al. 2009; Petty and Li 2013; Ebtehaj et al. 2015). In addition to the neighbor search algorithms relying on radiometric distances, some experimental algorithms implement different statistical learning approaches such as neural networks using the same a priori databases for the training (Tsintikidis et al. 1997; Sanò et al. 2015).

The database can be seen as an ensemble of points in the N-dimensional radiometric space (N being the length of the TB vectors, i.e., the number of channels of the imager) where the hydrometeor profile and the surface precipitation rate R are defined. Therefore, for each new radiometric observation, the retrieval of the surface precipitation can be seen as an interpolation problem. However, because different hydrometeor profiles may have very similar or identical spectral signatures (Figs. 1a,b), the function $R(\mathbf{TB})$ to interpolate is not regular (in the Lipchitz sense) meaning that $||\mathbf{TB}_i - \mathbf{TB}_j|| \rightarrow 0$ does not necessarily imply that $|R(\mathbf{TB}_i) - R(\mathbf{TB}_j)| \rightarrow 0$ (Fig. 1c). Therefore, even with a densely populated database, associating a radiometric observation to the hydrometeor profile of the database having the closest spectral signature may lead to substantial retrieval errors. For this reason, most retrieval algorithms provide smooth estimates of the surface precipitation rate by averaging or combining several profiles of the database having similar spectral signatures instead of associating the observed TB vector to a single hydrometeor profile. Bayesian versions of the retrieval, computing the a posteriori probability distribution of the precipitation rate given the observations, have also been developed to overcome the uncertainty issue (e.g., Evans et al. 1995; Kummerow et al. 2006; Chiu and Petty 2006). Under the Bayesian framework, one can retain the precipitation rate for which the a posteriori probability is maximal as the ''best'' estimate (maximum likelihood estimate). Alternatively, the expected value of the a posteriori distribution of R is the estimate that theoretically minimizes the mean squared error of the retrieval (minimum mean squared error estimator). Either way, these Bayesian smooth estimators tend to lessen the spatial and temporal variability of precipitation, with mitigation of the extreme values and the statistical distribution of the estimates having a lower variance than the true precipitation fields (provided that the a priori distribution of the precipitation rates is unimodal, with finite mean and variance) (DeGroot 2004; Foufoula-Georgiou et al. 2014).

As already stated, a large part of the final uncertainty on the retrieval is inherent to the incompleteness of the information provided by the vector of observed TBs. When computing the variograms of $R(\mathbf{TB})$ in the TB space, this inherent uncertainty appears as a nugget effect (Cressie 1993) (Fig. 1c) and therefore, it cannot be reduced by increasing the density of the retrieval database (or by increasing the size of the training dataset for deep learning algorithms). It is also independent of the distance metric used to compute the distances between the TB vectors. The only way to reduce this uncertainty is to add supplementary information to the vector of observed TBs. This may be achieved by using ancillary datasets, as for example environmental variables from reanalyses (Ferraro et al. 2005; Ringerud et al. 2015; Kidd et al. 2016; Petković et al. 2018; Takbiri et al. 2019).

While the current state-of-the-art algorithms may rely on ancillary data to contextualize the observed TB vectors, they do not use the context information provided by the TB fields themselves. Indeed, the retrieval is performed one pixel at a time and independently for

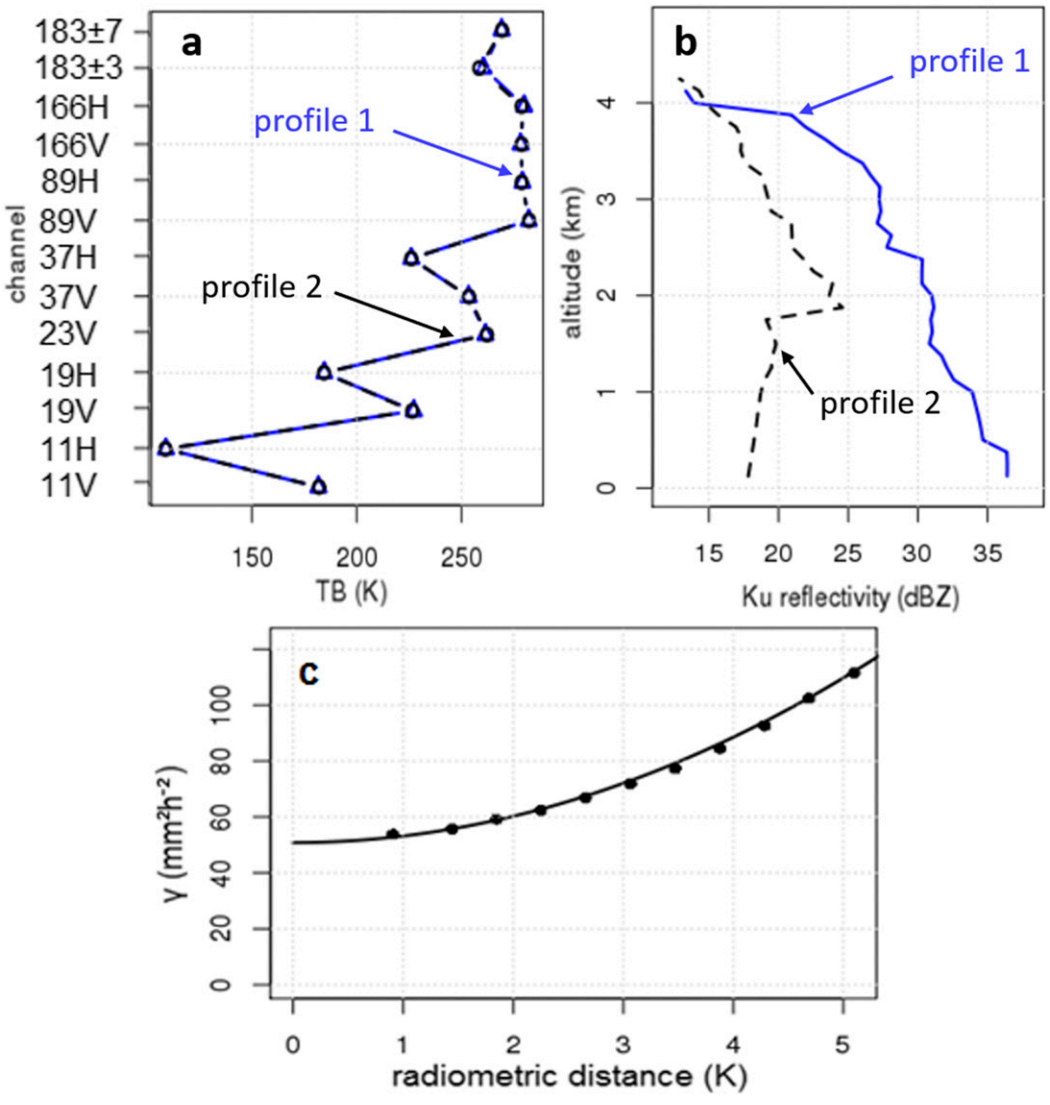

FIG. 1. Atmospheric profiles with quasi-identical spectral signatures can have very different radar reflectivity profiles and surface rain rates. (a) Two spectral signatures measured by GMI over ocean and (b) corresponding Ku reflectivites measured by the DPR along GMI's field of view. The profile 1 was observed at latitude −3.29° and longitude 170.89° at 1210 UTC 6 Sep 2016 (orbit 14342 of the GPM *Core Observatory*) and has a 15 mm h^{-1} surface precipitation rate. The profile 2 was observed at latitude 2.49° and longitude −136.25° at 1730 UTC 4 Dec 2015 (orbit 10036) and has a 1 mm h^{-1} surface precipitation rate. (c) Variogram of the function $R(\mathbf{TB})$ in the 13-dimensional space of TBs derived from 4000 collocated GMI-measured radiometric vectors $\mathbf{TB}_i$ [all within a 5 K radiometric distance from the two vectors shown in (a)] and DPR-derived surface precipitation rate R_i over ocean. The variogram shows the expected value of the squared difference $1/2 \times |R(\mathbf{TB}_i) - R(\mathbf{TB}_j)|^2$ as a function of the Euclidean distance $||\mathbf{TB}_i - \mathbf{TB}_j||$. The so-called "nugget effect" [expected squared difference $|R(\mathbf{TB}_1) - R(\mathbf{TB}_2)|^2$ not tending toward zero when the distance $||\mathbf{TB}_1 - \mathbf{TB}_2||$ tends toward zero (Cressie 1993)] quantifies the inherent uncertainty of the retrieval and is solely attributed to the limited radiometric information. The nugget effect accounts for 52% of the variance of R among the 4000 hydrometeor profiles, the total sample variance being 98 mm^2 h^{-2} and the sample mean 13.1 mm h^{-1}.

all pixels; that is, each pixel is retrieved only from the TBs measured at the corresponding location and all the neighboring TBs are ignored. Some algorithms have used statistical indices computed over a restrained neighborhood around the pixel of interest to identify cloud type and precipitation type. For example, Prabhakara et al. (2000), and later Gopalan et al. (2010), used the minimum value and the standard deviation of the TB at 85 GHz within a 40 km neighborhood to estimate the convection fraction at the pixel of interest. However, these indices

have only been used for unispectral or bispectral algorithms within a linear regression framework so far. What is proposed here is to exploit the information contained in the observed fields of TB by analyzing spatial variations, covariations and patterns of TBs at various scales instead of associating a TB signature to a hydrometeor profile at the ''pixel'' level as is classically done. Several elements related to the observation geometry and the scale dependence of the relations between precipitation and TBs motivate our resolve to overcome the pixel-wise approach of the retrieval by developing a new ''nonlocal'' approach. These elements are detailed and supported by examples in this article. The article is organized as follows: section 2 is dedicated to the description of the used data, namely brightness temperatures from the GMI instrument collocated with observations from the Dual-Frequency Precipitation Radar (DPR) on board the GPM *Core Observatory* satellite. In section 3, the observation geometry of GMI and other similar passive microwave imagers is described, with particular focus on how this geometry interacts with the three-dimensional structure of precipitation, making the pixel and the resolution of the retrieval not trivial to define. In section 4, relations between measured TBs and precipitation are analyzed in terms of their spatial patterns and scale dependence. Preliminary results on the reduction of the retrieval uncertainty allowed by using nonlocal information, namely spatial derivatives (gradients) and spatial averages of TBs at various scales, are presented in section 5, while conclusions and perspectives are discussed in section 6.

2. Data

The analysis presented in this article relies on the brightness temperatures measured by the GMI on board the GPM *Core Observatory* satellite collocated with the measurements from the DPR also on board the GPM *Core Observatory*.

a. GMI brightness temperature

The GMI instrument on board the GPM *Core Observatory* (Draper et al. 2015) measures the radiances originating from the atmosphere and Earth's surface below the satellite. Vertically polarized radiances are measured at 10.6, 18.7, 23.8, 37, 89, and 166 GHz (single-band channels), and at 183 ± 3 GHz and 183 ± 7 GHz (double-sideband channels). Horizontally polarized radiances are measured at 10.6, 18.7, 37, 89, and 166 GHz (single-band channels). In the following, the notation 37V designates the 37 GHz vertically polarized channel, the notation 89H designates the 89 GHz horizontally polarized channel, etc. The GMI scan is conical with a constant 53° Earth incidence angle covering an approximately 850-km wide swath. More details on GMI's observation geometry and on its consequence on the retrieval of precipitation are given in section 3. The GPM *Core Observatory* performs 16 orbits per day covering latitudes between 0° and ±65°. Its orbit is non-sun-synchronous, so the local time of the overpasses is variable. In this article, the brightness temperatures derived from the radiances measured by the 13 channels of GMI distributed by NASA under the GPM_1CGPMGMI_R.05 product (GPM GMI Common Calibrated Brightness Temperatures Collocated L1C version 5) are used (Berg 2016).

b. DPR reflectivity and near-surface precipitation rate

The DPR instrument is made of two radars operating at 13.6 GHz (Ku band) and 35.5 GHz (Ka band). For the statistical analyses performed in this article, only the reflectivities and precipitation rates from the Ku-band Precipitation Radar (KuPR) are used. The KuPR cross-track scan covers 245 km wide swath embedded within the wider swath of GMI. The radar produces three-dimensional reflectivity profiles of the atmosphere below 22 km altitude with a 250 m vertical resolution and a 5 km horizontal resolution. The minimum reflectivity measurable by the KuPR is 12 dBZ. In this article, attenuation-corrected reflectivities and radar-derived near-surface precipitation rates from the GPM_2AKu.06 product (GPM DPR Ku Precipitation Profile 2A version 6) (Iguchi and Meneghini 2016a) are used. Ka and Ku/Ka combined precipitation estimates are not used in the present study because the narrower swath of the KaPR (120 km) limits the number of profiles that can be collocated with GMI observations and the extent over which spatial patterns analysis can be performed.

c. GPROF passive-microwave-derived near-surface precipitation rate

GPROF is the operational NASA Precipitation Profiling algorithm for the passive microwave imagers of the GPM constellation (Kummerow et al. 2015). The GPROF version 5 near-surface precipitation rate estimates from the GMI instrument (GPM_2AGPROFGPMGMI.05 product) (Iguchi and Meneghini 2016b) are used in this article as reference state-of-the-art passive microwave estimates. The surface classes defined by Aires et al. (2011) and the 2-m temperature from the ECMWF interim reanalysis (ERA-Interim) used as input of the GPROF algorithm are also used for the analyses presented in this study; these two variables are provided as ancillary data in the GPM_2AGPROFGPMGMI.05 product files.

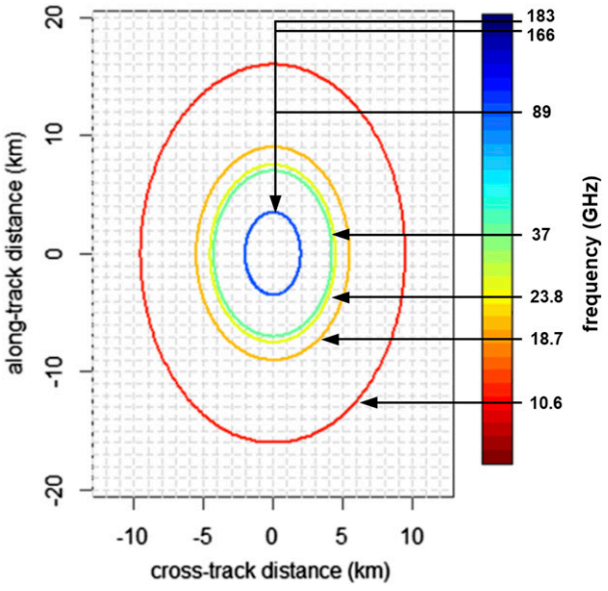

FIG. 2. The −3 dB footprints of GMI at 10.6, 18.7, 23.8, 37, 89, 166, and 183 GHz. Because of varying footprints of the different GMI channels, defining the retrieval pixel and resolution is not trivial. We note that same-frequency vertically and horizontally polarized channels have identical footprints and that the 166 and 183 GHz channels have the same footprint size as the 89 GHz channels.

3. Observation geometry and definition of the retrieval pixel

We describe below the observation geometry of the GMI on board the GPM *Core Observatory* satellite. GMI continuously measures the radiations coming from the surface and the atmosphere below the GPM *Core Observatory* satellite. For the 9 lower-frequency channels (between 10 and 90 GHz) the mechanical rotation of GMI allows to perform a conical scan at a constant 53° Earth incidence angle over an around 850-km wide swath every 1.9 s. Each scan is made of 221 samples, 5 km apart. The distance between two consecutive scans (along-track) is 13.5 km. Each sample corresponds to a different position of the observation beam (or field of view) for each one of the 9 channels. While all 9 beams are concentric for a given sample, the beamwidth varies with the frequency; the footprint, defined as the intersection of the −3 dB beam contour with the surface is then different for each channel (Fig. 2). The 4 higher-frequency channels of GMI have a slightly different scanning geometry compared to the lower frequencies, with beams centered at different locations (Draper et al. 2015). In the GPM_1CGPMGMI_R.05 product used in this article, the measured TBs at 166 and 183 GHz are interpolated at the locations of the low-frequency observations.

The state-of-the-art algorithms perform the retrieval of the local precipitation rate at the intersection of the beams with the surface for each individual sample from the 13 measured TBs. One must note that the fact that each channel has its own footprint creates an issue for the definition of the pixel and resolution of the retrieval. Some retrieval products (arbitrarily) assign the retrieval pixel to the footprint of one of the channels or to an average footprint compromising between the different channel footprints (Munchak and Skofronick-Jackson 2013). A computational footprint matching method relying on convolution and deconvolution operators has been proposed by Petty and Bennartz (2017) to generate synthetic footprints converging toward the 18.7 GHz footprint for all GMI channels. While the method performs reasonably well for the 23.8 and 37 GHz channels, it is less satisfactory for the 10.6 and 89 GHz channels.

One shall also consider the fact that for a given channel, the gain of the receiving antenna (i.e., the sensitivity of the imager) is not constant inside the footprint. While the footprints are classically defined as the intersection of the surface with the −3 dB contour of the antenna beam this definition is also partially arbitrary; the −6 dB contour is sometimes used as an alternative for defining radiometric footprints (e.g., Cracknell 1992; Kucera et al. 2004) (for a Gaussian beam 75% of the transmitted/received power is focused inside the −3 dB contour and 90% inside the −6 dB contour). Regardless of the definition of the retrieval pixel, the assumption that the measured TBs respond to the average precipitation rate inside this pixel is always a very crude approximation. In the end, when establishing statistical relationships between measured TBs and precipitation rates or constructing a priori databases for precipitation retrieval, the resolution at which the rain rates are computed is at the discretion of the algorithm developers.

While the target variable of the retrieval is generally the precipitation rate at the surface, the observed TBs are sensitive to the presence of hydrometeors at any altitude in the atmospheric column (Bauer et al. 1998; Fu and Liu 2001; You et al. 2015; Guilloteau et al. 2018). In fact, in addition to the surface precipitation rate, various parameters characterizing the observed atmospheric column (e.g., integrated liquid/ice water content, precipitation top height, etc.) can be retrieved from the passive microwave TBs (Bauer and Schluessel 1993; Ferraro et al. 2005; Tapiador et al. 2019). One must note that with the 53° Earth incidence angle of GMI, the observed atmospheric volume for each individual sample is not a vertical but rather a tilted column, which may lead to very heterogeneous and seemingly inconsistent distribution of the hydrometeors inside the observed volume. This is also prone to create a dependence of the measured TBs on the azimuthal direction of the observation (Bauer et al. 1998; Hong et al. 2000). The consequence of this is

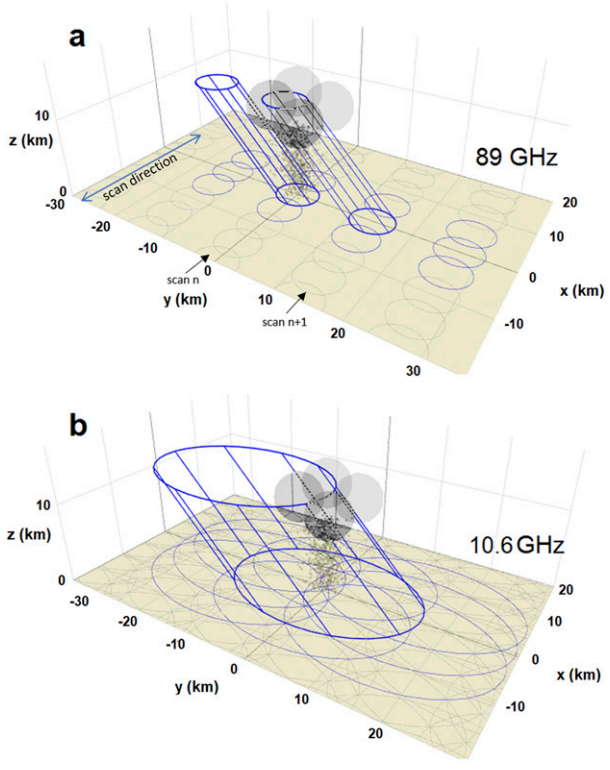

FIG. 3. Illustration of split and shifted multispectral information from the observation geometry. (a) GMI three-dimensional observation geometry at 89 GHz. The cylinders correspond to the fields of view (−3 dB contour) of individual TB measurements. Here, two fields of view intercepting the same atmospheric column at different altitudes are represented. The footprints corresponding to several adjacent fields of view are shown on the surface. (b) GMI three-dimensional observation geometry at 10.6 GHz. With the overlapping of the fields of view, a single atmospheric column is intercepted up to 12 times at 10.6 GHz.

that two systems with different spatial structure and different precipitation rates observed from different directions may give rise to similar measured TBs. Additionally, with such a geometry, at a given frequency, a given vertical atmospheric column is always intercepted by several beams at various altitude levels (Fig. 3a). Moreover, with different channels responding to the presence of hydrometeors at different altitude levels, the multispectral signature characterizing a given vertical column may be split across several samples. In particular, the signature of the atmospheric ice is likely to appear in beams intercepting the column at a high altitude rather than in the beam intercepting the column at the ground level; this effect is called parallax shift and is documented in several publications (Bauer et al. 1998; Guilloteau et al. 2018). Additionally, significant overlapping of adjacent fields of view occurs for frequencies lower than 40 GHz. For GMI, at 10.6 GHz, a given atmospheric column may be intercepted by up to 12 different beams (Fig. 3b).

From these geometrical considerations, neighboring TBs are expected to contain information complementary to that of the local TBs and potentially useful for retrieving precipitation in the pixel of interest. Actually, for the high-frequency channels responding to ice particles at high altitude, because of the parallax shift caused by the 53° Earth incidence angle of the scan, the TBs measured in one or several neighbor pixels are potentially more informative than the local TB for the retrieval of the local precipitation rate (Guilloteau et al. 2018). More generally, with the high incidence angle of the observations, the three-dimensional variability of precipitation systems, including their vertical variability is likely to be partially reflected in the variations of the two-dimensional fields of observed TB. We note that the considerations made here about GMI are also valid for other conical-scanning microwave imagers such as SSMIS on board the DMSP satellite series (Kunkee et al. 2008) or AMSR-2 on board the *GCOM-W1* satellite (Imaoka et al. 2012) which also have an Earth incidence angle of around 53°, frequency-dependent beamwidths and overlapping fields of view.

4. Pattern signature and scale-dependence of the TB–precipitation relations

Because of the observation geometry and instrumental characteristics mentioned in the previous section, the pixel size and spatial resolution of the retrieval of the surface precipitation rate are partially arbitrarily defined [see Guilloteau et al. (2017) for a detailed discussion on the resolution and "effective resolution" of passive microwave retrievals]. Additionally, pixel-wise relations between TBs and precipitation are limited in the sense that they do not account for the fact that precipitation fields are spatially organized at several scales and that the response of the TBs to the spatial variability of precipitation is complex and scale-dependent. Moreover, while some spectral signatures can be ambiguous at the pixel level, the analysis of the spatial patterns of the TBs may allow to partially resolve this ambiguity. In other words, some specific atmospheric features are expected to generate specific spatial patterns (or geometric signatures) rendering them more easily identifiable in the TB fields. We present here two case studies illustrating this fact.

The first case study is identified through the analysis of a database of 4 million GPM KuPR radar reflectivity profiles and near-surface precipitation rates over ocean, associated to collocated GMI TB vectors at the pixel level. One of the reflectivity profiles of this database, showing a 149 mm h^{-1} precipitation rate at the surface (average rate in the 18.7 GHz GMI −3 dB footprint) is associated to a 278 K brightness temperature at 89 GHz

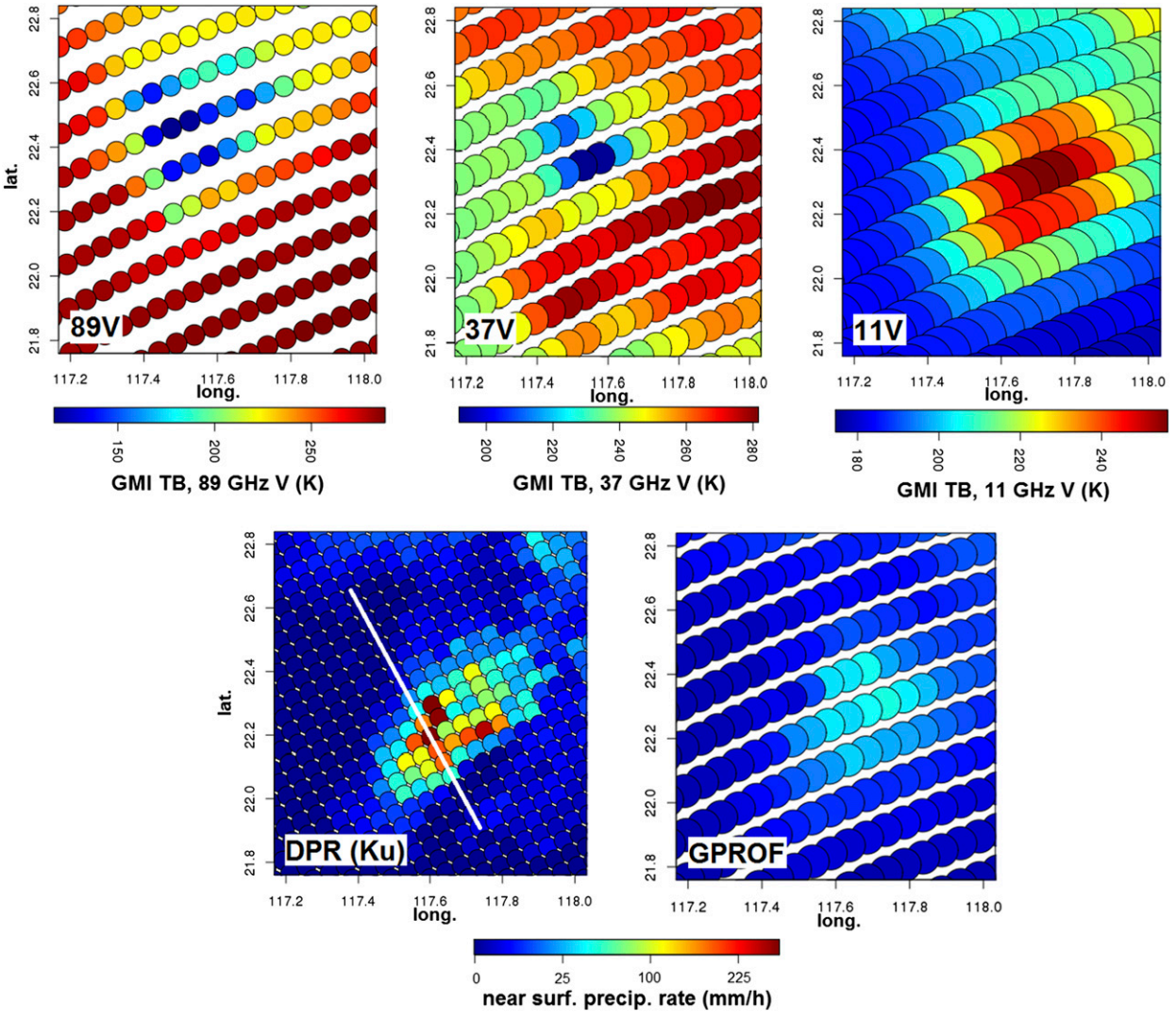

FIG. 4. Exploration of the information in the spatial structure of the GMI TBs for an oceanic convective system (South China Sea, at 0445 UTC 9 Oct 2016). (top) Observed TBs at 89, 37, and 10.6 GHz (vertical polarization). (bottom) Near-surface precipitation rates derived from the DPR and from GMI using the GPROF algorithm; the white line corresponds to the cross section shown in Fig. 5. The ice scattering signature at 89 GHz is shifted to the northwest relatively to the emission signature at 10.6 GHz; this shift and the spatial structure of the TB fields in general reflect the three-dimensional structure of the precipitation field (see Fig. 5). This example illustrates the need to overcome pixel-wise relations between TBs and precipitation by using the spatial information of the TB fields.

(vertical polarization). Such a high TB at 89 GHz indicates that the observed atmospheric column contains no (or few) ice particles. The absence of a significant amount of ice is very surprising as liquid-phase only precipitation processes are unlikely to generate instantaneous precipitation rates higher than 50 mm h^{-1} (Liu and Zipser 2009; Lebsock and L'Ecuyer 2011). In fact, precipitation rates as high as 149 mm h^{-1} are expected to be associated with convective systems showing radar echo tops several kilometers above the melting layer (Tokay et al. 1999; Hamada et al. 2015). This particular profile was observed over the South China Sea at latitude 22.1° and longitude 17.7° at 0445 UTC 9 October 2016 (orbit 14851 of the GPM *Core Observatory*). Figure 4 shows the GMI-observed fields of TB at 10.6, 37, and 89 GHz (vertical polarization) in the vicinity of this profile, as well as the near-surface precipitation fields derived from the TBs using the NASA operational algorithm GPROF and the near-surface precipitation derived from the DPR. The above-mentioned profile is located near the southeastern edge of a 60 km by 30 km area with extremely intense radar near-surface precipitation rates (higher than 60 mm h^{-1} and locally higher than 200 mm h^{-1}). The high TBs (between 225 and 260 K)

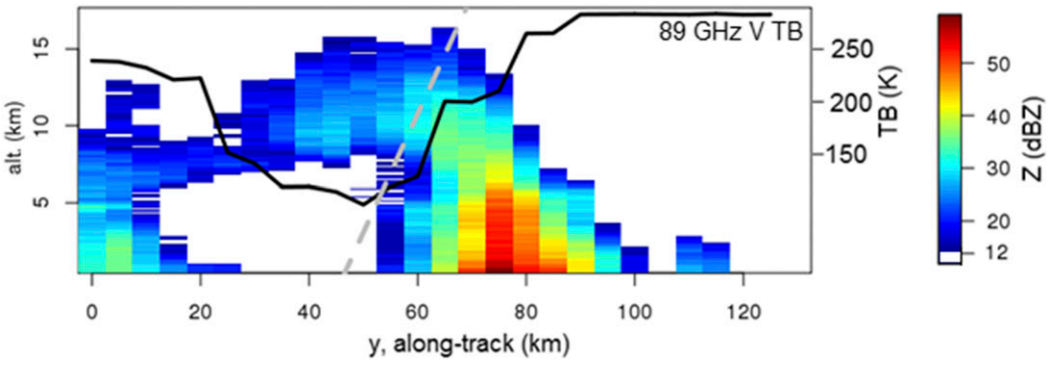

FIG. 5. DPR Ku reflectivity vertical cross section of the precipitation system shown in Fig. 4. The system is a tilted deep convective system. The cross section is taken along the azimuthal direction of the GMI beams. The gray dashed line shows the direction of GMI's observations. The black line shows GMI-measured 89 GHz V TB (scale on the right). The tilt amplifies the parallax shift causing the spatial mismatch between the liquid drops emission signature and the ice scattering signature in the TB fields.

measured by GMI at 10.6 GHz inside this area, indicating strong emission from liquid rain drops, are consistent with the radar observations.

We noticed previously the absence of ice scattering signature at 89 GHz in a pixel where the DPR-estimated surface precipitation rate is 149 mm h^{-1}. In fact, a 180-K depression caused by the ice scattering actually appears in the 89 GHz TB field, about 40 km northwest from the location of maximum DPR near-surface precipitation rate. It is interesting to note that the location of the maximum of the 89 GHz TB depression corresponds to a zero-precipitation area according to the DPR. The analysis of the three-dimensional structure of the precipitation system seen by the DPR reveals a deep convective system with an echo top above 15 km altitude (Fig. 5). It can be seen that the maximum of the radar reflectivity above 10 km altitude is horizontally shifted by about 20 km relatively to the location of the maximum near-surface reflectivity because the system has a tilted vertical structure. Additionally, the parallax effect, caused by the Earth incidence angle of the passive microwave imager associated with the fact that the 89 GHz TB responds primarily to the presence of ice in the upper layer of the clouds generates a shift between the apparent location of the ice-scattering signature at 89 GHz and the actual location of the ice clusters. This shift is proportional to the mean altitude of the center of gravity of the ice (Bauer et al. 1998; Guilloteau et al. 2018). In the present case study, the parallax shift is on the order of 15–20 km and adds to the physical horizontal shift between the high-altitude ice cluster and the maximum of the near-surface precipitation. Hong et al. (2000) also analyzed tilted convective systems observed by aircraft and ground-based radars and spaceborne microwave imagers (TMI and SSM/I) and reported shifts up to 100 km between the maximum of the liquid emission signal and the maximum of the ice scattering signal.

The estimated precipitation field derived from the passive microwave observations with the GPROF algorithm shows a correct location of the precipitation at the surface but also a severe underestimation of the precipitation rate. The GPROF algorithm successfully associates the emission signal at 10–40 GHz with the precipitating area, but, with the absence of a significant ice scattering signal in the corresponding pixels, it fails to identify the extremely active deep convective cell. The geometric mismatch between the emission signal and the scattering signal therefore penalizes the retrieval. Nevertheless, the observed spatial shift between the liquid emission signal at 10.6 GHz and the ice-scattering signal at 89 GHz potentially provides information about the underlying structure of the observed precipitation system, revealing in particular its vertical development; however, an algorithm relying only on pixel-wise relations between TB and precipitation cannot leverage this information.

The interpretation of the spatial patterns of the brightness temperature can be particularly informative for channels that are sensitive to both ice scattering and liquid emission. This is the case in particular for the 37 GHz channels of GMI. In the present case study, the combination of the ice scattering and liquid emission signals generates a strong TB gradient at 37 GHz between the area where the emission signal is dominant and the area where the scattering signal is dominant (Fig. 4). Because of the 53° Earth incidence angle of GMI, this gradient reveals both the horizontal and vertical structure of the precipitation system. One must note that, because the area where the surface precipitation is the most intense is located at the limit between the areas of strong ice scattering and strong liquid emission, it shows moderately high TBs at 37 GHz, similar to those observed in areas with low precipitation rates. One can also note that the shift between the maximum of the ice scattering signal

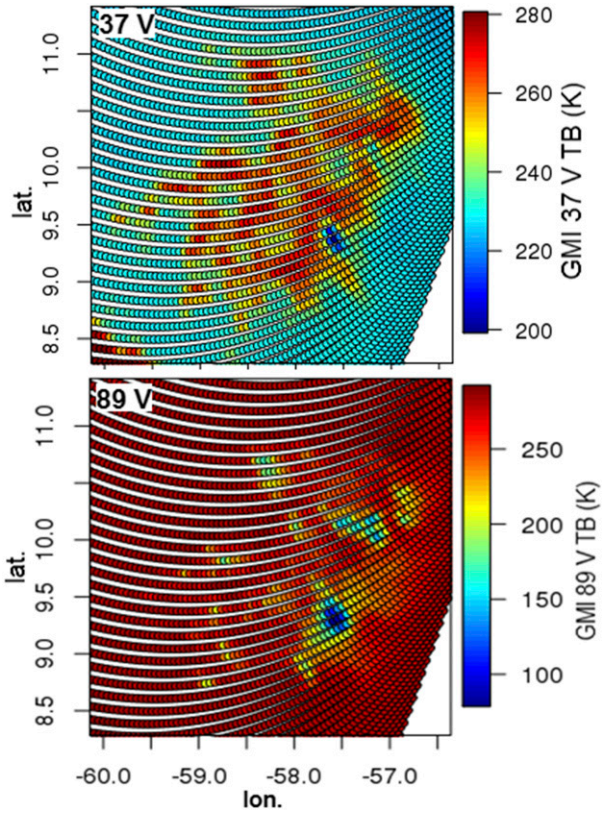

FIG. 6. Mesoscale convective complex observed by GMI at 37 and 89 GHz (vertical polarization) over the Atlantic Ocean at 0640 UTC 9 Oct 2016. At 37 GHz the high TB envelope marks the extent of the precipitating area. Inside this envelope, local depressions of the TB at 89 and 37 GHz mark the most intense convective cells.

and the maximum of the surface precipitation rate is smaller at 37 GHz than at 89 GHz, which can be explained by the fact that the 37 GHz channel is sensitive to larger ice particles found at lower altitudes.

The second case study illustrates more specifically the particularity of the 37 GHz channels, which are sensitive to both liquid raindrops emission and ice scattering. [One must note that all channels are potentially sensitive to both phenomena, however the emission signal is generally dominant for frequencies lower than 30 GHz and the scattering signal is dominant for frequencies higher than 50 GHz (Liu and Curry 1992)]. Because of this, the 37 GHz TBs have a nonmonotonic response to the intensity of precipitation (Spencer 1986): the absence of precipitation is associated with medium TBs, low or medium precipitation rates are associated with high TBs, high convective precipitation rates are associated with medium TBs and extreme deep convective precipitation rates are associated with low TBs. Figure 6 shows a tropical mesoscale convective system observed by GMI at 37 and 89 GHz over the Atlantic Ocean off the coast of Brazil at 0640 UTC 9 October 2016 (orbit 14852). At 37 GHz the system appears as a 300 km by 300 km area with an average TB higher than 245 K (while the TB of the ocean in the surrounding precipitation-free area is around 230 K). Strong variations of the 37 GHz TB can be observed within the system with TBs locally higher than 275 K and several areas of low or medium TBs (230–250 K) embedded inside a larger region with relatively high mean TB. A strong depression of the 37 GHz TB can be observed at the southeastern edge of the system, reaching a minimum value lower than 200 K. At 89 GHz, identifying the extent of the precipitating area is uneasy, but one can observe depressions of the TB caused by ice scattering at several locations coinciding with local minima of the 37 GHz TB. This indicates that the variations of the 37 GHz TB inside the system are mostly caused by the ice scattering rather than resulting from variations of the liquid rain drops emission signal.

From this last case study, it seems that while the coarse-scale variations of the 37 GHz TB (i.e., spatial averages over large areas) are dominated by the liquid drops emission signal, finescale local variations (intrasystem variability) is dominated by the ice-scattering signal. Statistics at the global scale confirm this finding. The coefficient of linear correlation between the 37V and 89V TBs computed from 4 years of GMI measurements over ocean (see Fig. 7a) is −0.08 (excluding nonprecipitating areas). Both TBs are corrected from the influence of the surface temperature (assimilated to the ERA-Interim 2-m temperature), assuming a linear relation between TB and surface temperature [see appendix B and Guilloteau et al. (2018) for more details]. While from the previous result the 37 and 89 GHz TBs do not appear to be linearly correlated, after removing the finescale spatial variations in both TB fields through low-pass filtering (convolution with a Gaussian smoothing kernel, with $\sigma = 30$ km) we find a −0.47 correlation coefficient between the two TBs (Fig. 7b). On the contrary, if we apply a high-pass filtering (isotropic Laplacian of Gaussian differentiating kernel, with $\sigma = 15$ km), we find a positive 0.24 correlation between the two TBs (Fig. 7c). Assuming that the 89 GHz TB responds essentially to ice scattering at all scales, this confirms that the finescale variability of the 37 GHz TB in precipitating areas is dominated by the ice-scattering signal, while the coarse-scale variability is dominated by the liquid rain drops emission signal. Once again, this illustrates the complexity of the scale-dependent relations between the TBs and precipitation, which if understood and quantified can be leveraged for improved retrieval.

While inferring a precipitation regime and precipitation rate from the pixel value of the 37 GHz TB may not always be possible because of the ambiguous nonmonotonic relation between the two variables, the analysis of the

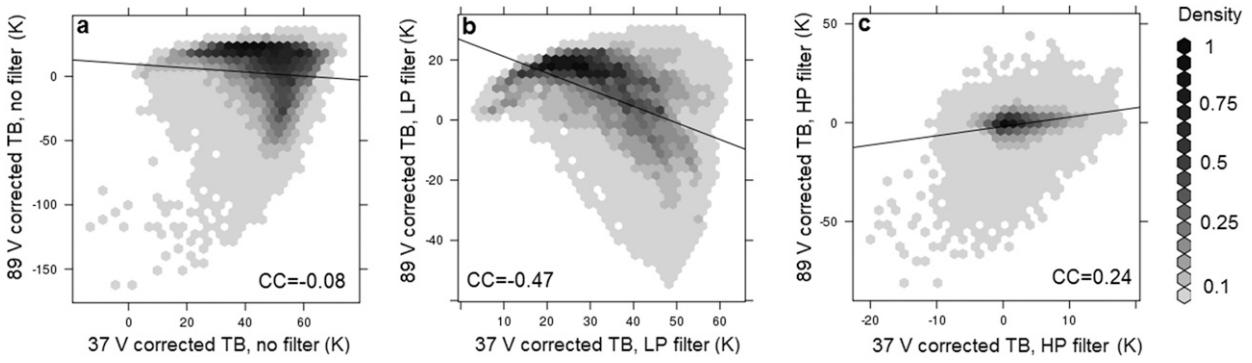

FIG. 7. Scale dependence in the statistical relations between the 37 and 89V TBs in precipitating areas over ocean. (a) Joint distribution of TBs 37 and 89V observed by GMI in precipitating areas over ocean; (b) joint distribution of TBs 37 and 89V after low-pass spatial filtering (convolution with a Gaussian kernel with $\sigma = 30$ km) of both TBs; and (c) joint distribution of TBs 37 and 89V after high-pass spatial filtering (isotropic Laplacian of Gaussian kernel with $\sigma = 15$ km) of both TBs. See Szeliski (2010) for the description of the Gaussian and Laplacian of Gaussian kernels. The correlation between the 37 and 89V TBs is negative for the coarse scale gradients and positive for the finescale gradients. The correlation coefficients are computed from 70 000 randomly sampled independent data points over global ocean and are all statistically significant at the 99% level. All TBs are corrected for surface temperature variations before applying the filtering [see appendix B and Guilloteau et al. (2018)].

spatial pattern of the 37 GHz TB field can help resolve the ambiguity. For example, an area of medium or low TBs embedded inside an area of high TBs is a typical pattern signature of a deep convective cell, generally associated with high precipitation rates. Convective cells are also prone to appear as dipoles in the 37 GHz TB fields, with a local maximum caused by liquid emission close to a local minimum caused by ice scattering. Even if the system is not tilted, the emission and scattering signals may be spatially shifted because of the incidence angle of the microwave imager. This may be beneficial for retrieval as it prevents the scattering and emission signals at 37 GHz from cancelling each other out.

5. Extracting nonlocal parameters for enriched radiometric information and reduced retrieval uncertainty

The results presented in the previous section show that the spatial patterns of the TBs potentially contain useful information for retrieving hydrometeor profiles and estimating the surface precipitation rate. Convolution filters are a widely used potent tool for the analysis of the spatial variations and patterns in images or physical fields (Milligan and Gunn 1997; Szeliski 2010). For numerical images, the filtering operation simply consists of convolving the image with a convolution matrix (or kernel). Various standardized types of kernels exist, enabling blurring, smoothing and sharpening, as well as edge and pattern extraction with or without dependence on directionality. Some families of convolution kernels such as wavelets, designed for multiresolution analysis (Kumar and Foufoula-Georgiou 1997) are potentially useful for analyzing and utilizing the scale-dependent relations between TBs and precipitation (Turiel et al. 2005; Guilloteau et al. 2017; Klein et al. 2018). We call a "nonlocal radiometric parameter" the result of the convolution of the TB field with a predefined kernel at a given location. For each pixel and for each radiometric channel many different nonlocal parameters can be computed using different convolution kernels. Including these nonlocal parameters in the a priori database allows for a more comprehensive radiometric characterization of each individual hydrometeor profile of the database.

For algorithms relying on the computation of the radiometric distance between the observation and the profiles of the a priori database, the nonlocal parameters can then be used to form enriched radiometric vectors and compute the radiometric distances in a higher-dimensional space. This is expected to partially resolve the ambiguity between radiometric signatures and hydrometeor profiles, allowing to distinguish previously indistinguishable hydrometeor profiles from the enriched radiometric information. While many different nonlocal radiometric parameters can potentially be computed, a parsimonious parameterization is always preferable for computational efficiency. Moreover, for a retrieval based on radiometric distance, it is also preferable to keep the number of dimensions of the radiometric space low enough to ensure that the radiometric vectors of the database stay reasonably close to each other (Beyer et al. 1999).

As a proof of concept, a simple k-nearest neighbors retrieval algorithm (Hastie et al. 2009) has been implemented using two 700 000-member a priori databases of DPR hydrometeor profiles associated with collocated GMI radiometric measurements. The first database

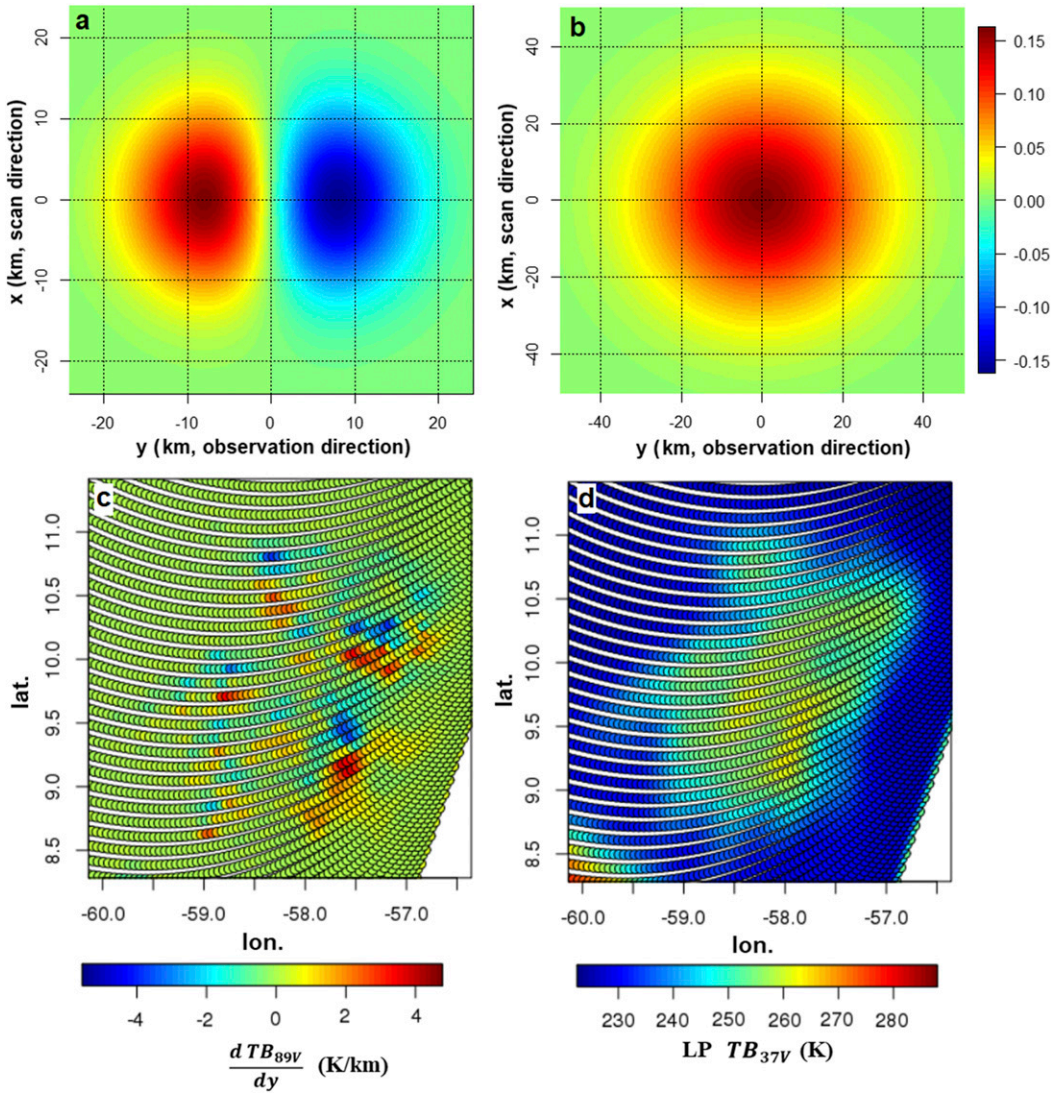

FIG. 8. Convolution kernels used to extract spatial information from the TB fields. (a) First derivative of Gaussian kernel (Szeliski 2010): $f(x, y) = -(y/2\pi\sigma^4)e^{-[(x^2+y^2)/2\sigma^2]}$ with $\sigma = 8$ km; this kernel is convolved with the 37 and 89V TB fields. (b) Gaussian kernel (Szeliski 2010): $f(x, y) = (1/2\pi\sigma^2)e^{-[(x^2+y^2)/2\sigma^2]}$ with $\sigma = 20$ km; this kernel is convolved with the 37 V TB field. (c) Result of the convolution of the 89V TB field shown in Fig. 6 (bottom) with the First derivative of Gaussian kernel. (d) Result of the convolution of the 37V TB field shown in Fig. 6 (top) with the Gaussian kernel. The Gaussian smoothing kernel partially erases the ice-scattering signal at 37 GHz. In (a) and (b), the x direction is tangent to the imager's scan (orthogonal to the observation direction) and the y direction is along the azimuthal direction of the imager's observation beam (orthogonal to the scan).

contains only profiles over vegetated land surfaces, excluding, in particular, coastal areas and snow-covered areas. For this, we rely on the surface type classification used in the current operational implementation (V05) of the GPROF algorithm (Aires et al. 2011). The vegetated surface classes account for 70% of all land surfaces at the latitudes covered by the GPM *Core Observatory*. The second database contains only profiles over ocean. Each profile of the two databases is associated with the 13 TBs between 10 and 183 GHz measured by GMI, the 2-m temperature derived from the ERA-Interim reanalysis, and 3 nonlocal radiometric parameters. The k-nearest neighbors search is therefore performed in a 17-dimensional space.

The first two nonlocal parameters are chosen to characterize the spatial derivative of the 37V and 89V TBs in the azimuthal direction of GMI's observation beam. These two parameters are obtained by convolving the 37V and 89V TB fields with a first derivative of Gaussian kernel (with $\sigma = 8$ km, Fig. 8a). Figures 9a and 9b shows

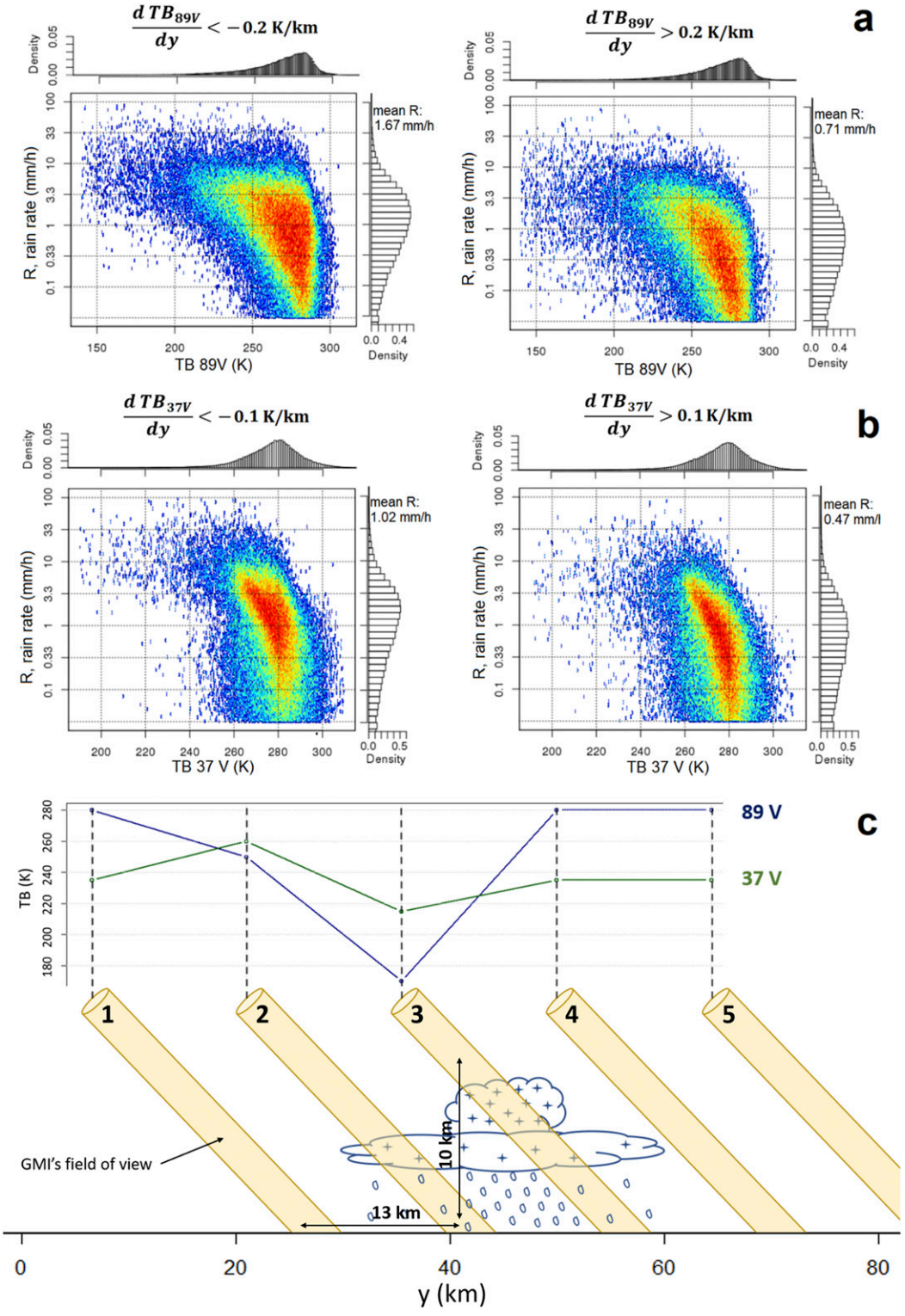

FIG. 9. (a) Joint distributions of DPR surface rain rates and collocated GMI 89V TBs conditioned on the value of the spatial derivative (gradient) of the 89V TB in the azimuthal direction of GMI's observation beam over land: for (left) negative, and (right) positive gradients. (b) Joint distributions of DPR surface rain rates and collocated GMI 37V TBs conditioned on the value of the spatial derivative (gradient) of the 37V TB in the azimuthal direction of GMI's observation beam over land: for (left) negative, and (right) positive gradients. (c) Schematic illustration of

that, over land, the statistical relations between surface precipitation rate and the local value of the 37V and 89V TBs vary significantly when conditioned on the value of the two nonlocal parameters; in particular, they vary depending on the sign of these two parameters. For example, when the spatial derivative of the 89V TB in the azimuthal direction of the beam is negative, the precipitation rate is on average 2.4 times higher than when the derivative is positive (while the conditional marginal distribution of the local 89V TB is identical for the two cases). A similar result is found with the spatial derivative of the 37V TB. This asymmetry is the consequence of the tilted observation beam of GMI as illustrated in Fig. 9c. In fact, the 37 and 89V TB gradients partially reflect the vertical variability of the precipitating system. The most intense precipitation rates are more likely to be found in the areas where the gradient is negative, that is, when a lower 37V and/or 89V TB is measured in the next field of view in the azimuthal direction of the observation (which intercepts the same atmospheric column 10 km higher), as this is likely to indicate the presence of ice particles at high altitude. Including the 37V and 89V directional gradients in the retrieval scheme is expected to help differentiating precipitating systems which have different three-dimensional structure but show similar spectral signatures when observed from different azimuthal angles. It is also expected to allow identifying profiles which are potentially affected by the parallax shift effect.

The third parameter is obtained by convolving the 37 V TB field with a Gaussian low-pass filtering kernel (with $\sigma = 20$ km, Fig. 8b). This parameter is expected to characterize the liquid rain emission signal at 37 GHz by removing the finescale spatial variations associated with the ice scattering (Fig. 8d); consequently, the difference between this parameter and the raw 37 GHz TB is expected to characterize the ice-scattering signal only.

The target variable of the k-nearest neighbors retrieval is the average near-surface precipitation rate inside the 18.7 GHz −3 dB footprint of GMI. For each new radiometric observation over land or over ocean, the radiometric distance to each profile of the corresponding database is computed as a Euclidean distance:

$$D_{o,i} = \|\mathbf{V}_i - \mathbf{V}_o\|,$$

where $\mathbf{V}_o$, belonging to $\mathbb{R}^{17}$, is the observed radiometric vector made of the 13 GMI TBs (pixel values), plus the 2-m temperature and the 3 nonlocal radiometric parameters; $\mathbf{V}_i$, belonging to $\mathbb{R}^{17}$, is the corresponding radiometric vector associated with the ith profile of the a priori database (with i belonging to $\{1, 2, \ldots, 7 \times 10^5\}$). The k profiles of the database for which $D_{o,i}$ is minimal are retained and the final estimate of the near-surface precipitation rate R_{GMI} is simply the mean value (without weighting) of the k near-surface radar-derived precipitation rates R_{DPR} associated to these k profiles. This extremely simple retrieval scheme is used to demonstrate that the nonlocal parameters contain information useful to reduce the retrieval uncertainty. The use of nonlocal parameters in a neighbor-search algorithm does not require defining explicit relations between TB patterns and precipitation; it is simply assumed that similar TB patterns correspond to similar precipitation systems and geometries. In particular, with this approach, it is not necessary to explicitly correct for the parallax shift as is done in Guilloteau et al. (2018).

The retrieval performance is evaluated over 6 million randomly sampled DPR profiles and collocated GMI TBs (3 million profiles over ocean and 3 million profiles over land, all independent from those of the retrieval databases), with k varying between 1 and 28. For comparison, the retrieval is also performed without including the nonlocal parameters in the vectors $\mathbf{V}_o$ and $\mathbf{V}_i$, thus computing the radiometric distances $D_{o,i}$ in a 14-dimensional space (13 GMI TBs plus the 2-m temperature). Figure 10 (top) shows the mean absolute retrieval error [mean absolute difference between the GMI-retrieved precipitation rate and the DPR Ku precipitation rate $E(|R_{\mathrm{GMI}} - R_{\mathrm{DPR}}|)$ with $|\cdot|$ denoting the absolute value] as a function of k with and without using the nonlocal parameters. One can see that, for all values of k, the inclusion of the three nonlocal parameters allows a reduction of the mean absolute error of around 11% over land and around 6% over ocean. Additionally, it can be seen that the same level of mean absolute error

←

GMI's observation geometry for a typical convective system. The observation geometry causes the asymmetrical relationship between TB gradients and precipitation rates at 37 and 89 GHz. The area of maximum precipitation rate (between the fields of view 2 and 3) corresponds to decreasing TB gradients along the observation direction. The distributions of (a) and (b) are obtained from 700 000 randomly sampled collocated DPR and GMI observations over vegetated surfaces (coastal areas and snow-covered areas excluded). Precipitation rates correspond to near-surface KuPR-derived precipitation rates averaged inside GMI's −3 dB footprint at 18.7 GHz.

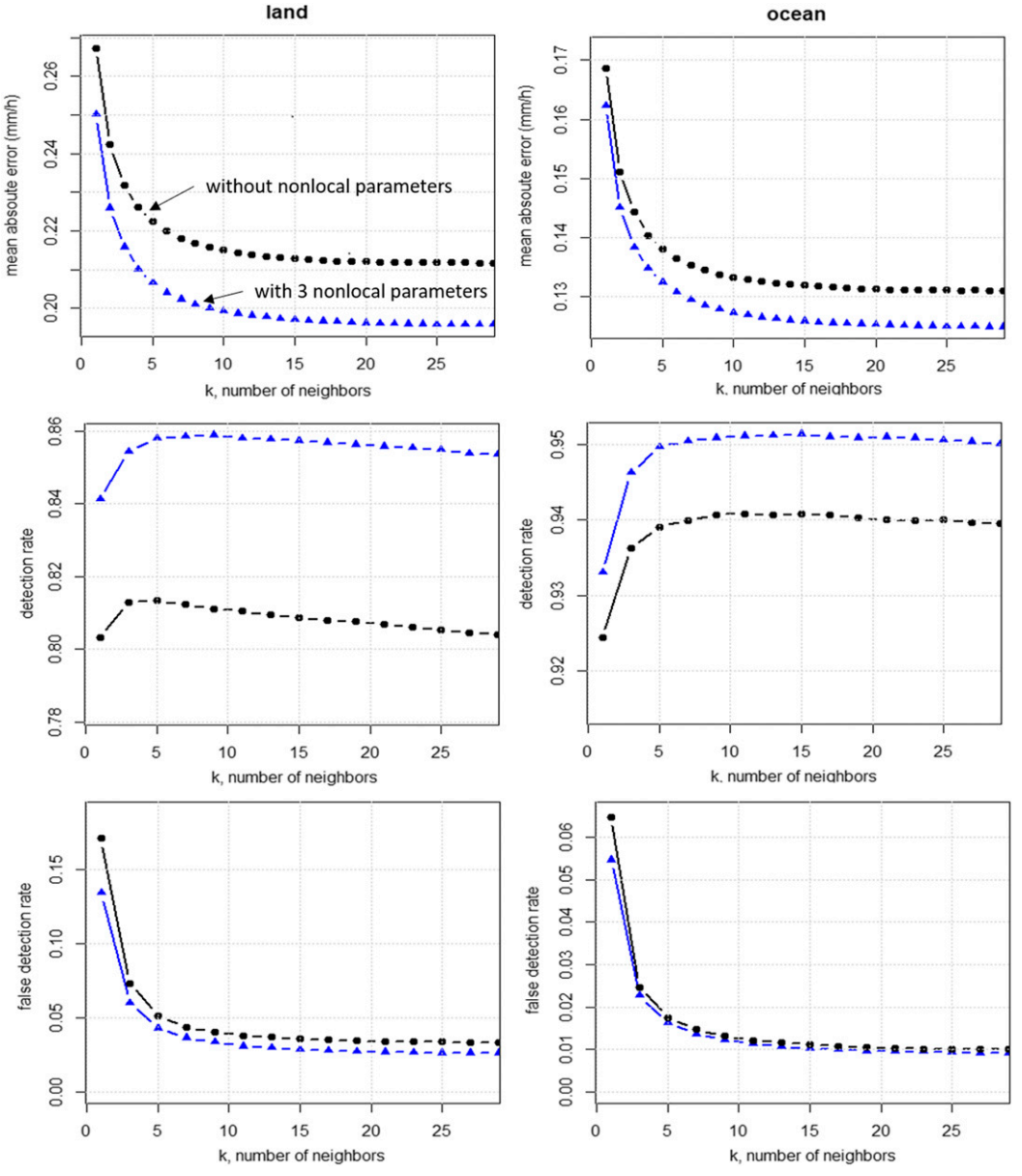

FIG. 10. Comparison of the retrieval performance of the k-nearest neighbors algorithm with and without the nonlocal parameters. (top) Mean absolute error of the retrieved near-surface precipitation rate over land and ocean as a function of the number k of neighbors retained in the nearest-neighbor algorithm for two different retrieval schemes: using 13 TBs plus the 2-m temperature (black circles); and using 13 TBs plus the 2-m temperature plus 3 nonlocal radiometric parameters (blue triangles). (middle) Detection rate over land and ocean as a function of k with (blue triangles) and without (black circles) the three nonlocal radiometric parameters. (bottom) False detection rate over land and ocean as a function of k with (blue triangles) and without (black circles) the three nonlocal radiometric parameters. The three nonlocal parameters are the spatial derivative of the 37 and 89V TBs in the azimuthal direction of the beam (from a first derivative of Gaussian convolution kernel with $\sigma = 8$ km) and the low-pass-filtered 37V TB (using a smoothing Gaussian convolution kernel with $\sigma = 20$ km). Note that the detection rate and false detection rate are computed only for odd values of k.

can be reached with a smaller value of k, that is, a less smooth estimate for the retrieval using the nonlocal information. For k greater than 15, the mean absolute error is found stable around 0.195 mm h^{-1} over land and around 0.124 mm h^{-1} over ocean. For comparison, the mean absolute errors for the GPROF estimates on the same test datasets are respectively 0.266 and 0.154 mm h^{-1}.

The ability of nonlocal parameters to help the k-nearest neighbors algorithm distinguishing between precipitating and nonprecipitating profiles is also tested. The observed scene is considered precipitating if the majority of the k profiles of the retrieval database selected by the k-nearest neighbors algorithm are associated to a nonzero surface precipitation rates (with a $0.3\,\mathrm{mm\,h^{-1}}$ detection threshold). This is implemented only with odd values of k to avoid indecisive results (i.e., 50% of the k profiles being precipitating profiles). Significant improvement of the detection rate (percentage of precipitating profiles correctly identified) is observed over both ocean and land surfaces when including the nonlocal parameters: from 81% to 86% over land and 94% to 95% over ocean (Fig. 10, middle). In terms of false detection rate (percentage of profiles classified as precipitating by k-nearest neighbors algorithm which are nonprecipitating according to the radar), the improvement is faint over ocean. Over land, when k is higher than 15, the false detection rate is reduced from 3.6% to 2.6% (Fig. 10, bottom). This improvement in detection performance can be attributed to a better localization of the edges of the systems allowed by the nonlocal parameters. Considering that the two evaluation datasets are made of 3 million independent profiles, for all the considered scoring metrics (mean retrieval error, detection rate and false detection rate) the improvement is statistically significant at the 99% level.

Figure 11 shows that the reduction of the mean absolute error due to incorporation of the nonlocal parameters affects the retrieval of stratiform-type precipitation as well as convective-type precipitation. Precipitation type is determined from the KuPR reflectivity profile using the Awaka et al. (1997), method. A microwave pixel is classified as stratiform (convective) if 60% or more of the 18.7 GHz footprint is classified as stratiform (convective) from the KuPR. All other precipitating profiles are classified as mixed or undetermined precipitation type. While over land the nonlocal parameters allow only very little improvement for stratiform-type precipitation, the reduction of the mean absolute error is noticeable for convective-type precipitation and is particularly salient for mixed/undetermined precipitation type. Over ocean, the improvement is more salient for stratiform and mixed/undetermined precipitation types than for convective precipitation.

6. Conclusions and perspectives

The retrieval of surface precipitation from passive microwave observations is intrinsically uncertain to some degree because of the limited information content of the radiometric measurements. In the present article, we illustrate via case studies the fact that the relations between TBs and precipitation constructed at the pixel level are limited by the fact that 1) due to the observation geometry, the multispectral information characterizing the local state of the atmosphere can be spatially shifted and split across several neighboring pixels and 2) the relations between TBs and precipitation can be nonmonotonic and scale dependent. These results motivate a new direction for passive microwave precipitation retrieval that moves away from the pixel-wise only approach and considers the spatial patterns and variations/covariations of TBs at various scales. We call it a nonlocal retrieval approach and note that although it is potentially pertinent for the remote sensing of any spatial variable, it is particularly relevant for vertically integrated atmospheric measurements, as the observed horizontal variability may partially reflect the vertical variability of the underlying process (horizontal and vertical variations being dynamically coupled).

From a global analysis over land and ocean, we show that using standard convolution filters (Gaussian and derivative of Gaussian) to extract nonlocal parameters from the TB fields allows to define enriched spectral signatures that can help resolve the ambiguity in the TB-precipitation relations. In particular, at 37 GHz, scale-dependent information extracted through convolution filters enables to partially separate the liquid drops emission signal from the ice scattering signal, the latter being associated with finer-scale variations. The nonlocal parameters are also useful in handling the complex observation geometry of conical-scanning microwave imagers. For example, considering the spatial derivative of the ice-sensitive TBs (higher than 30 GHz) in the azimuthal direction of the imager's observation beam helps characterizing the vertical variability of hydrometeor profiles and handling the parallax shift effect.

Initial results show that adding only three nonlocal parameters to the vector of TBs for the computation of the radiometric distances in a k-nearest neighbors retrieval scheme allows improving the retrieval performance scores over ocean and land surfaces. Over land, the detection rate is improved from 81% to 86%, the false alarm ratio is reduced from 3.6% to 2.6% and the mean absolute error is reduced from 0.212 to $0.195\,\mathrm{mm\,h^{-1}}$. Over ocean, the detection rate is improved from 94% to 95% and the mean absolute error is reduced from 0.132 to $0.124\,\mathrm{mm\,h^{-1}}$, all improvements being statistically significant. While improvement is noticed for the retrieval of both stratiform and convective type precipitation, the most significant improvement occurs when the precipitation type is not homogeneous within the 18.7 GHz footprint or when the precipitation type could not be determined by the radar algorithm, that is, for atypical

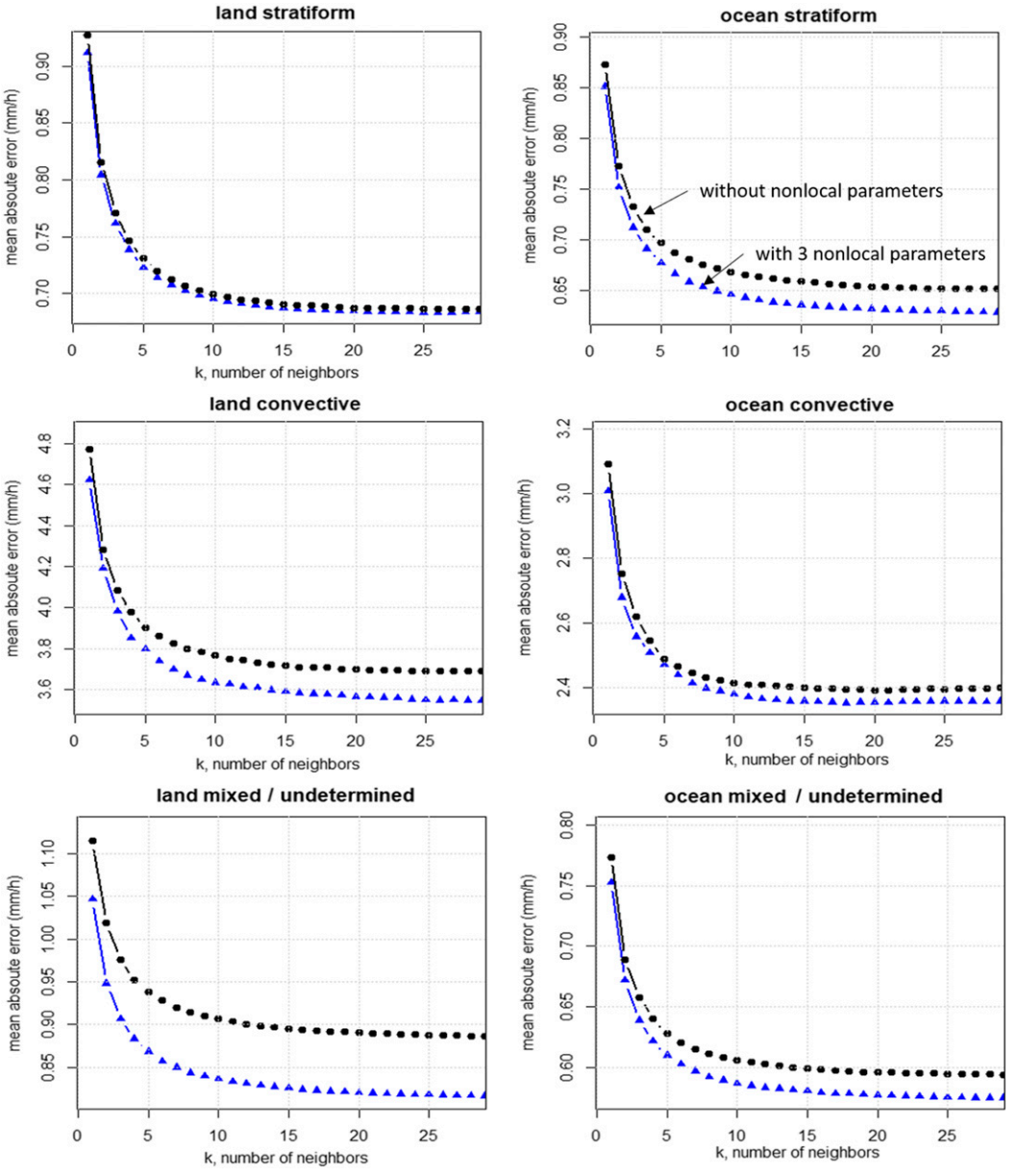

FIG. 11. Mean absolute error of the retrieved near-surface precipitation rate over (left) land and (right) ocean, for (top) stratiform, (middle) convective, and (bottom) mixed/undetermined hydrometeor profiles, as a function of the number k of neighbors retained by the nearest-neighbor algorithm for two different retrieval schemes: using 13 TBs plus the 2-m temperature (black circles); and using 13 TBs plus the 2-m temperature plus 3 nonlocal radiometric parameters (blue triangles). The number of stratiform, convective and mixed/undetermined profiles is respectively 301934, 30931, 188657 over land, and 233194, 21133, 172254 over ocean. The class of hydrometeor profile is determined from the KuPR reflectivity profile using the Awaka et al. (1997) method. A profile is classified as stratiform (convective) if 60% or more of the 18.7 GHz footprint is classified as stratiform (convective). All other precipitating profiles are classified as mixed or undetermined precipitation type.

profiles, which are known to be challenging for passive microwave precipitation retrievals.

The interpretation of the TB fields is always easier over ocean than over land surfaces because of the complex varying background emission of land surfaces. In particular, the surface emissivity makes the interpretation of the low-frequency liquid emission-sensitive TBs notably complicated over land surfaces. Therefore, passive microwave retrieval over land relies preferably on the high-frequency ice-scattering signal. It must be

noted that, although the illustrative case studies presented in section 4 are oceanic systems, the three nonlocal parameters retained for the retrieval demonstration essentially improve the characterization of the ice-scattering signal, allowing a more salient improvement of the retrieval over land surfaces (11% reduction of the mean absolute retrieval error against 6% over ocean). Scale decomposition and pattern extraction may also help distinguishing the atmospheric signal from the background surface signal over land. The addition of more than three nonlocal parameters in the *k*-nearest neighbors retrieval scheme (not shown) was not found to further improve the retrieval in terms of global statistics; however, this may be due to the limited ability of the *k*-nearest neighbors algorithm to handle high-dimensional problems. The patterns at 166 and 183 GHz in particular are expected to contain information similar to the 89 GHz patterns with potentially higher benefits for the identification of small ice particles and of falling snow. One shall note that the nonlocal parameters used here for the initial demonstration are the same over land and ocean; however, surface-specific fine-tuning and parameter optimization is likely to allow further improvement of the retrieval performance and this is a topic for future research.

Apart from the nonlocal parameters extracted with linear convolution filters examined in this study, various methods can also be explored for extracting nonlocal information from the fields of TB and to determine an optimal set of parameters in terms of both parsimony and information content (Hastie et al. 2009). For example, as an alternative to the heuristic approach used here within a *k*-nearest neighbors retrieval framework, learning via neural networks, which has already been successfully used for the retrieval of precipitation from passive instruments (Hsu et al. 1997; Hong et al. 2004; Sanò et al. 2015), offers an attractive alternative in terms of extracting pattern information. The results of the present study advocate in particular for the use of deep convolutional neural networks, a class of neural networks using convolution filters (Lecun et al. 2015; Nogueira et al. 2017). However, a prior comprehensive analysis of the retrieval problem and of the available datasets is always necessary to guide the machine learning approach (e.g., to help choose the topology of a neural network).

One of the arguments for the necessity of overcoming the pixel-wise approach of precipitation retrieval from passive microwave sensors is the spatial shift between the liquid rain drops emission signal and the ice scattering signal. As already noted by Hong et al. (2000), this effect is naturally more salient when the instrumental resolution is higher. Consequently, higher instrumental resolution may paradoxically be disadvantageous for the retrieval of precipitation, and particularly for the retrieval of the finescale variability with a pixel-wise retrieval scheme. The nonlocal retrieval approach proposed herein may therefore allow to realize the full benefits of the increased resolution and accuracy of the most recent and future microwave imagers.

We presented herein the use of nonlocal parameters to enrich the spectral signatures derived from the conical-scanning passive microwave imager GMI (on board the GPM *Core Observatory* satellite) specifically designed for the retrieval of precipitation. It must be noted that precipitation can also be detected and measured from passive microwave imagers designed for other purposes such as the cross-track scanning humidity sounders MHS and SAPHIR (Kidd et al. 2016). Because these instruments have fewer channels than GMI, in particular they miss the low-frequency channels sensitive to liquid drops emission and the polarization information, the (pixel-wise) spectral signatures they produce have a poorer information content regarding precipitation. Therefore, the incremental gain of using nonlocal parameters to retrieve precipitation from these types of instruments is potentially higher than for the conical-scanning microwave imagers such as GMI, SSMI/S, and AMSR-2. One must note that multisensor precipitation products such as CMORPH (Xie et al. 2017), IMERG (Huffman et al. 2018), or GSMaP-MVK (Ushio et al. 2009), providing global mapping of hourly or half-hourly cumulative precipitation, rely on instantaneous precipitation retrievals from both conical-scanning imagers and cross-track sounders. Thus, exploring the nonlocal retrieval approach holds great potential for improving the accuracy and space–time resolution of multisensor merged products.

Acknowledgments. This work was supported by the NASA Global Precipitation Measurement Program under Grants NNX16AO56G and 80NSSC19K0684 and by NSF Grants DMS-1839336 and ECCS-1839441. The authors thank Prof. Christian Kummerow, Dr. Dave Randel, and Dr. Wesley Berg from the Precipitation Group at the Colorado State University as well as Dr. Joseph Turk from NASA Jet Propulsion Laboratory for the insightful discussions and shared information which contributed to the present article.

APPENDIX A

Acronyms

AMSR-2	Advanced Microwave Scanning Radiometer 2
CMORPH	Climate Prediction Center morphing technique
DMSP	Defense Meteorological Satellite Program

DPR	Dual-Frequency Precipitation Radar
ECMWF	European Centre for Medium-Range Weather Forecasts
ERA	ECMWF Re-Analysis
GCOM-W1	*Global Change Observation Mission–Water*
GMI	GPM Microwave Imager
GPM	Global Precipitation Measurement
GPROF	Goddard profiling algorithm
GSMaP-MVK	Global Satellite Mapping of Precipitation with Moving Vectors and Kalman filtering
IMERG	Integrated Multisatellite Retrievals for GPM
KuPR	Ku Precipitation Radar
MHS	Microwave Humidity Sounder
NASA	National Aeronautics and Space Administration
SAPHIR	Sondeur Atmosphérique du Profil d'Humidité Intertropicale (atmospheric sounder for intertropical humidity profile)
SMMR	Scanning Multichannel Microwave Radiometer
SSM/I	Special Sensor Microwave Imager
SSMIS	Special Sensor Microwave Imager/Sounder
TB	Brightness Temperature
TMI	TRMM Microwave Imager
TRMM	Tropical Rainfall Measuring Mission

APPENDIX B

Correcting Observed TBs from the Influence of the Surface Temperature

The method used in Guilloteau et al. (2018) to correct GMI's 89V TBs from the influence of the surface temperature is used here over ocean for the 89V and 37V channels. In nonprecipitating areas, two linear regressions are performed between GMI 37V TB and ERA-Interim 2-m temperature and between the 89V TB and the 2-m temperature. We establish the following relations between TB_{37V}, TB_{89V}, and T_{2m} expressed in kelvin in nonprecipitating areas:

$$TB_{37V\_NP} = 31.15 + 0.595\,T_{2m} \quad \text{(B1)}$$

and

$$TB_{89V\_NP} = -117.12 + 1.248\,T_{2m}. \quad \text{(B2)}$$

We define the corrected 37V and 89V TBs as

$$TB_{37V\_cor} = TB_{37V} - TB_{37V\_NP} \quad \text{(B3)}$$

and

$$TB_{89V\_cor} = TB_{89V} - TB_{89V\_NP}. \quad \text{(B4)}$$

The corrected TBs are expected to vary only due to hydrometeors and should have a value close to 0 K for nonprecipitating profiles.

REFERENCES

Aires, F., C. Prigent, F. Bernardo, C. Jiménez, R. Saunders, and P. Brunel, 2011: A Tool to Estimate Land-Surface Emissivities at Microwave frequencies (TELSEM) for use in numerical weather prediction. *Quart. J. Roy. Meteor. Soc.*, **137**, 690–699, https://doi.org/10.1002/qj.803.

Awaka, J., T. Iguchi, H. Kumagai, and K. Okamoto, 1997: Rain type classification algorithm for TRMM precipitation radar. *Proc. IEEE Int. Conf. on Geoscience and Remote Sensing Symp. 1997*, Singapore, Institute of Electrical and Electronics Engineers, 1633–1635, https://doi.org/10.1109/IGARSS.1997.608993.

Bauer, P., and P. Schluessel, 1993: Rainfall, total water, ice water, and water vapor over sea from polarized microwave simulations and special sensor microwave/imager data. *J. Geophys. Res.*, **98**, 20 737–20 759, https://doi.org/10.1029/93JD01577.

——, L. Schanz, and L. Roberti, 1998: Correction of three-dimensional effects for passive microwave remote sensing of convective clouds. *J. Appl. Meteor.*, **37**, 1619–1632, https://doi.org/10.1175/1520-0450(1998)037<1619:COTDEF>2.0.CO;2.

——, P. Amayenc, C. D. Kummerow, and E. A. Smith, 2001: Over-ocean rainfall retrieval from multisensor data of the Tropical Rainfall Measuring Mission. Part II: Algorithm implementation. *J. Atmos. Oceanic Technol.*, **18**, 1838–1855, https://doi.org/10.1175/1520-0426(2001)018<1838:OORRFM>2.0.CO;2.

Berg, W., 2016: GPM GMI_R Common Calibrated Brightness Temperatures Collocated L1C 1.5 hours 13 km V05, version 5. Goddard Earth Sciences Data and Information Services Center (GES DISC), accessed 1 November 2019, https://doi.org/10.5067/GPM/GMI/R/1C/05.

Beyer, K., J. Goldstein, R. Ramakrishnan, and U. Shaft, 1999: When is ''nearest neighbor'' meaningful? *Database Theory–ICDT'99*, C. Beeri and P. Buneman, Eds., Lecture Notes in Computer Science, Vol. 1540, Springer, 217–235.

Chiu, J. C., and G. W. Petty, 2006: Bayesian retrieval of complete posterior PDFs of oceanic rain rate from microwave observations. *J. Appl. Meteor. Climatol.*, **45**, 1073–1095, https://doi.org/10.1175/JAM2392.1.

Cracknell, A. P., 1992: Passive microwave techniques. *Space Oceanography: An Intensive Course*, World Scientific, 321–354.

Cressie, N., 1993: Geostatistical data. *Statistics for Spatial Data*, Wiley, 21–381.

DeGroot, M. H., 2004: *Optimal Statistical Decisions*. John Wiley and Sons, 489 pp.

Draper, D. W., D. A. Newell, F. J. Wentz, S. Krimchansky, and G. M. Skofronick-Jackson, 2015: The Global Precipitation Measurement (GPM) Microwave Imager (GMI): Instrument overview and early on-orbit performance. *IEEE J. Sel. Top. Appl. Earth Obs. Remote Sens.*, **8**, 3452–3462, https://doi.org/10.1109/JSTARS.2015.2403303.

Ebtehaj, A. M., R. L. Bras, and E. Foufoula-Georgiou, 2015: Shrunken locally linear embedding for passive microwave retrieval of precipitation. *IEEE Trans. Geosci. Remote Sens.*, **53**, 3720–3736, https://doi.org/10.1109/TGRS.2014.2382436.

Evans, K. F., J. Turk, T. Wong, and G. L. Stephens, 1995: A Bayesian approach to microwave precipitation profile retrieval. *J. Appl. Meteor.*, **34**, 260–279, https://doi.org/10.1175/1520-0450-34.1.260.

Ferraro, R. R., and G. F. Marks, 1995: The development of SSM/I rain-rate retrieval algorithms using ground-based radar measurements. *J. Atmos. Oceanic Technol.*, **12**, 755–770, https://doi.org/10.1175/1520-0426(1995)012<0755:TDOSRR>2.0.CO;2.

——, and Coauthors, 2005: NOAA operational hydrological products derived from the Advanced Microwave Sounding Unit. *IEEE Trans. Geosci. Remote Sens.*, **43**, 1036–1049, https://doi.org/10.1109/TGRS.2004.843249.

Foufoula-Georgiou, E., A. M. Ebtehaj, S. Q. Zhang, and A. Y. Hou, 2014: Downscaling satellite precipitation with emphasis on extremes: A variational ℓ_1-norm regularization in the derivative domain. *Surv. Geophys.*, **35**, 765–783, https://doi.org/10.1007/s10712-013-9264-9.

Fu, Y., and G. Liu, 2001: The variability of tropical precipitation profiles and its impact on microwave brightness temperatures as inferred from TRMM data. *J. Appl. Meteor.*, **40**, 2130–2143, https://doi.org/10.1175/1520-0450(2001)040<2130:TVOTPP>2.0.CO;2.

Gopalan, K., N. Y. Wang, R. Ferraro, and C. Liu, 2010: Status of the TRMM 2A12 land precipitation algorithm. *J. Atmos. Oceanic Technol.*, **27**, 1343–1354, https://doi.org/10.1175/2010JTECHA1454.1.

Guilloteau, C., E. Foufoula-Georgiou, and C. D. Kummerow, 2017: Global multiscale evaluation of satellite passive microwave retrieval of precipitation during the TRMM and GPM eras: Effective resolution and regional diagnostics for future algorithm development. *J. Hydrometeor.*, **18**, 3051–3070, https://doi.org/10.1175/JHM-D-17-0087.1.

——, ——, ——, and V. Petković, 2018: Resolving surface rain from GMI high-frequency channels: Limits imposed by the three-dimensional structure of precipitation. *J. Atmos. Oceanic Technol.*, **35**, 1835–1847, https://doi.org/10.1175/JTECH-D-18-0011.1.

Hamada, A., Y. N. Takayabu, C. Liu, and E. J. Zipser, 2015: Weak linkage between the heaviest rainfall and tallest storms. *Nat. Commun.*, **6**, 6213, https://doi.org/10.1038/ncomms7213.

Hastie, T., R. Tibshirani, and J. Friedman, 2009: *The Elements of Statistical Learning, Data Mining, Inference, and Prediction*. 2nd ed. Springer, 745 pp.

Hong, Y., J. L. Haferman, W. S. Olson, and C. D. Kummerow, 2000: Microwave brightness temperatures from tilted convective systems. *J. Appl. Meteor.*, **39**, 983–998, https://doi.org/10.1175/1520-0450(2000)039<0983:MBTFTC>2.0.CO;2.

——, K. L. Hsu, S. Sorooshian, and X. Gao, 2004: Precipitation estimation from remotely sensed imagery using an artificial neural network cloud classification system. *J. Appl. Meteor.*, **43**, 1834–1853, https://doi.org/10.1175/JAM2173.1.

Hou, A. Y., and Coauthors, 2014: The Global Precipitation Measurement mission. *Bull. Amer. Meteor. Soc.*, **95**, 701–722, https://doi.org/10.1175/BAMS-D-13-00164.1.

Hsu, K. L., X. Gao, S. Sorooshian, and H. V. Gupta, 1997: Precipitation estimation from remotely sensed information using artificial neural networks. *J. Appl. Meteor.*, **36**, 1176–1190, https://doi.org/10.1175/1520-0450(1997)036<1176:PEFRSI>2.0.CO;2.

Huffman, G. J., and Coauthors, 2018: NASA Global Precipitation Measurement (GPM) Integrated Multi-Satellite Retrievals for GPM (IMERG). Algorithm Theoretical Basis Doc., version 5.2, 31 pp., https://pmm.nasa.gov/sites/default/files/document_files/IMERG_ATBD_V5.2_0.pdf.

Iguchi, T., and R. Meneghini, 2016a: GPM DPR Ku Precipitation Profile 2A 1.5 hours 5 km V06, version 5. Goddard Earth Sciences Data and Information Services Center, accessed 1 November 2019, https://doi.org/10.5067/GPM/DPR/Ku/2A/06.

——, and ——, 2016b: GPM GMI (GPROF) Radiometer Precipitation Profiling L2A 1.5 hours 13 km V05, version 5. Goddard Earth Sciences Data and Information Services Center, accessed 1 November 2019, https://doi.org/10.5067/GPM/GMI/GPM/GPROF/2A/05.

Imaoka, K., T. Maeda, M. Kachi, M. Kasahara, N. Ito, and K. Nakagawa, 2012: Status of AMSR2 instrument on GCOM-W1. *Proc. SPIE*, **8528**, 852815, https://doi.org/10.1117/12.977774.

Kidd, C., T. Matsui, J. Chern, K. Mohr, C. Kummerow, and D. Randel, 2016: Global precipitation estimates from cross-track passive microwave observations using a physically based retrieval scheme. *J. Hydrometeor.*, **17**, 383–400, https://doi.org/10.1175/JHM-D-15-0051.1.

Klein, C., D. Belušić, and C. M. Taylor, 2018: Wavelet scale analysis of mesoscale convective systems for detecting deep convection from infrared imagery. *J. Geophys. Res. Atmos.*, **123**, 3035–3050, https://doi.org/10.1002/2017JD027432.

Kubota, T., and Coauthors, 2007: Global precipitation map using satellite-borne microwave radiometers by the GSMaP project: Production and validation. *IEEE Trans. Geosci. Remote Sens.*, **45**, 2259–2275, https://doi.org/10.1109/TGRS.2007.895337.

Kucera, P. A., W. F. Krajewski, and C. B. Young, 2004: Radar beam occultation studies using GIS and DEM technology: An example study of Guam. *J. Atmos. Oceanic Technol.*, **21**, 995–1006, https://doi.org/10.1175/1520-0426(2004)021<0995:RBOSUG>2.0.CO;2.

Kumar, P., and E. Foufoula-Georgiou, 1997: Wavelet analysis for geophysical applications. *Rev. Geophys.*, **35**, 385–412, https://doi.org/10.1029/97RG00427.

Kummerow, C., and L. Giglio, 1994: A passive microwave technique for estimating rainfall and vertical structure information from space. Part I: Algorithm description. *J. Appl. Meteor.*, **33**, 3–18, https://doi.org/10.1175/1520-0450(1994)033<0003:APMTFE>2.0.CO;2.

——, W. S. Olson, and L. Giglio, 1996: A simplified scheme for obtaining precipitation and vertical hydrometeor profiles from passive microwave sensors. *IEEE Trans. Geosci. Remote Sens.*, **34**, 1213–1232, https://doi.org/10.1109/36.536538.

——, and Coauthors, 2000: The status of the Tropical Rainfall Measuring Mission (TRMM) after two years in orbit. *J. Appl. Meteor.*, **39**, 1965–1982, https://doi.org/10.1175/1520-0450(2001)040<1965:TSOTTR>2.0.CO;2.

——, and Coauthors, 2001: The evolution of the Goddard profiling algorithm (GPROF) for rainfall estimation from passive microwave sensors. *J. Appl. Meteor.*, **40**, 1801–1820, https://doi.org/10.1175/1520-0450(2001)040<1801:TEOTGP>2.0.CO;2.

——, W. Berg, J. Thomas-Stahle, and H. Masunaga, 2006: Quantifying global uncertainties in a simple microwave rainfall algorithm. *J. Atmos. Oceanic Technol.*, **23**, 23–37, https://doi.org/10.1175/JTECH1827.1.

——, D. L. Randel, M. Kulie, N. Y. Wang, R. Ferraro, J. S. Munchak, and V. Petkovic, 2015: The evolution of the Goddard profiling algorithm to a fully parametric scheme. *J. Atmos. Oceanic Technol.*, **32**, 2265–2280, https://doi.org/10.1175/JTECH-D-15-0039.1.

Kunkee, D. B., G. A. Poe, D. J. Boucher, S. D. Swadley, Y. Hong, J. E. Wessel, and E. A. Uliana, 2008: Design and evaluation of the first special sensor microwave imager/sounder. *IEEE Trans. Geosci. Remote Sens.*, **46**, 863–883, https://doi.org/10.1109/TGRS.2008.917980.

Lebsock, M. D., and T. S. L'Ecuyer, 2011: The retrieval of warm rain from CloudSat. *J. Geophys. Res.*, **116**, D20209, https://doi.org/10.1029/2011JD016076.

Lecun, Y., Y. Bengio, and G. Hinton, 2015: Deep learning. *Nature*, **521**, 436–444, https://doi.org/10.1038/nature14539.

Liu, C., and E. J. Zipser, 2009: "Warm rain" in the tropics: Seasonal and regional distributions based on 9 yr of TRMM data. *J. Climate*, **22**, 767–779, https://doi.org/10.1175/2008JCLI2641.1.

Liu, G., and J. A. Curry, 1992: Retrieval of precipitation from satellite microwave measurement using both emission and scattering. *J. Geophys. Res.*, **97**, 9959–9974, https://doi.org/10.1029/92JD00289.

Löhnert, U., S. Crewell, C. Simmer, and A. Macke, 2001: Profiling cloud liquid water by combining active and passive microwave measurements with cloud model statistics. *J. Atmos. Oceanic Technol.*, **18**, 1354–1366, https://doi.org/10.1175/1520-0426(2001)018<1354:PCLWBC>2.0.CO;2.

Milligan, P. R., and P. J. Gunn, 1997: Enhancement and presentation of airborne geophysical data. *AGSO J. Aust. Geol. Geophys.*, **17**, 63–75.

Mugnai, A., and Coauthors, 2013: CDRD and PNPR satellite passive microwave precipitation retrieval algorithms: EuroTRMM/EURAINSAT origins and H-SAF operations. *Nat. Hazards Earth Syst. Sci.*, **13**, 887–912, https://doi.org/10.5194/nhess-13-887-2013.

Munchak, S. J., and G. Skofronick-Jackson, 2013: Evaluation of precipitation detection over various surfaces from passive microwave imagers and sounders. *Atmos. Res.*, **131**, 81–94, https://doi.org/10.1016/j.atmosres.2012.10.011.

Nogueira, K., O. A. B. Penatti, and J. A. dos Santos, 2017: Towards better exploiting convolutional neural networks for remote sensing scene classification. *Pattern Recognit.*, **61**, 539–556, https://doi.org/10.1016/j.patcog.2016.07.001.

Petković, V., C. D. Kummerow, D. L. Randel, J. R. Pierce, and J. K. Kodros, 2018: Improving the quality of heavy precipitation estimates from satellite passive microwave rainfall retrievals. *J. Hydrometeor.*, **19**, 69–85, https://doi.org/10.1175/JHM-D-17-0069.1.

Petty, G. W., 1994: Physical retrievals of over-ocean rain rate from multichannel microwave imagery. Part II: Algorithm implementation. *Meteor. Atmos. Phys.*, **54**, 101–121, https://doi.org/10.1007/BF01030054.

——, and K. Li, 2013: Improved passive microwave retrievals of rain rate over land and ocean. Part I: Algorithm description. *J. Atmos. Oceanic Technol.*, **30**, 2493–2508, https://doi.org/10.1175/JTECH-D-12-00144.1.

——, and R. Bennartz, 2017: Field-of-view characteristics and resolution matching for the Global Precipitation Measurement (GPM) Microwave Imager (GMI). *Atmos. Meas. Tech.*, **10**, 745–758, https://doi.org/10.5194/amt-10-745-2017.

Prabhakara, C., R. Iacovazzi Jr., J. A. Weinman, and G. Dalu, 2000: A TRMM microwave radiometer rain rate estimation method with convective and stratiform discrimination. *J. Meteor. Soc. Japan*, **78**, 241–258, https://doi.org/10.2151/jmsj1965.78.3_241.

Ringerud, S., C. D. Kummerow, and C. D. Peters-Lidard, 2015: A prototype physical database for passive microwave retrievals of precipitation over the US Southern Great Plains. *J. Geophys. Res. Atmos.*, **120**, 10 465–10 482, https://doi.org/10.1002/2015JD023430.

Sanò, P., D. Casella, A. Mugnai, G. Schiavon, E. A. Smith, and G. J. Tripoli, 2013: Transitioning from CRD to CDRD in Bayesian retrieval of rainfall from satellite passive microwave measurements: Part 1. Algorithm description and testing. *IEEE Trans. Geosci. Remote Sens.*, **51**, 4119–4143, https://doi.org/10.1109/TGRS.2012.2227332.

——, G. Panegrossi, D. Casella, F. Di Paola, L. Milani, A. Mugnai, M. Petracca, and S. Dietrich, 2015: The Passive microwave Neural network Precipitation Retrieval (PNPR) algorithm for AMSU/MHS observations: Description and application to European case studies. *Atmos. Meas. Tech.*, **8**, 837–857, https://doi.org/10.5194/amt-8-837-2015.

Skofronick-Jackson, G., and Coauthors, 2017: The Global Precipitation Measurement (GPM) mission for science and society. *Bull. Amer. Meteor. Soc.*, **98**, 1679–1695, https://doi.org/10.1175/BAMS-D-15-00306.1.

——, W. Berg, C. Kidd, D. B. Kirschbaum, W. A. Petersen, G. J. Huffman, and Y. N. Takayabu, 2018: Global Precipitation Measurement (GPM): Unified precipitation estimation from space. *Remote Sensing of Clouds and Precipitation*, C. Andronache, Ed., Springer, 175–193.

Spencer, R. W., 1986: A satellite passive 37-GHz scattering-based method for measuring oceanic rain rates. *J. Climate Appl. Meteor.*, **25**, 754–766, https://doi.org/10.1175/1520-0450(1986)025<0754:ASPGSB>2.0.CO;2.

——, H. M. Goodman, and R. E. Hood, 1989: Precipitation retrieval over land and ocean with the SSM/I: Identification and characteristics of the scattering signal. *J. Atmos. Oceanic Technol.*, **6**, 254–273, https://doi.org/10.1175/1520-0426(1989)006<0254:PROLAO>2.0.CO;2.

Szeliski, R., 2010: *Computer Vision: Algorithms and Applications*. Springer, 812 pp.

Takbiri, Z., A. Ebtehaj, E. Foufoula-Georgiou, P. E. Kirstetter, and F. J. Turk, 2019: A prognostic retrieval approach for microwave precipitation phase detection over snow cover. *J. Hydrometeor.*, **20**, 251–274, https://doi.org/10.1175/JHM-D-18-0021.1.

Tapiador, F. J., R. Moreno, and Z. S. Haddad, 2019: Estimates of the precipitation top heights in convective systems using microwave radiances. *IEEE Trans. Geosci. Remote Sens.*, **57**, 3166–3178, https://doi.org/10.1109/TGRS.2018.2882002.

Tokay, A., D. A. Short, C. R. Williams, W. L. Ecklund, and K. S. Gage, 1999: Tropical rainfall associated with convective and stratiform clouds: Intercomparison of disdrometer and profiler measurements. *J. Appl. Meteor.*, **38**, 302–320, https://doi.org/10.1175/1520-0450(1999)038<0302:TRAWCA>2.0.CO;2.

Tsintikidis, D., J. L. Haferman, E. N. Anagnostou, W. F. Krajewski, and T. F. Smith, 1997: A neural network approach to estimating rainfall from spaceborne microwave data. *IEEE Trans. Geosci. Remote Sens.*, **35**, 1079–1093, https://doi.org/10.1109/36.628775.

Turiel, A., J. Grazzini, and H. Yahia, 2005: Multiscale techniques for the detection of precipitation using thermal IR satellite images. *IEEE Geosci. Remote Sens. Lett.*, **2**, 447–450, https://doi.org/10.1109/LGRS.2005.852712.

Ushio, T., and Coauthors, 2009: A Kalman filter approach to the Global Satellite Mapping of Precipitation (GSMaP) from combined passive microwave and infrared radiometric data. *J. Meteor. Soc. Japan*, **87A**, 137–151, https://doi.org/10.2151/jmsj.87A.137.

Wilheit, T. T., and A. T. C. Chang, 1980: An algorithm for retrieval of ocean surface and atmospheric parameters from the observations of the scanning multichannel microwave radiometer. *Radio Sci.*, **15**, 525–544, https://doi.org/10.1029/RS015i003p00525.

——, ——, and L. S. Chiu, 1991: Retrieval of monthly rainfall indices from microwave radiometric measurements using probability distribution functions. *J. Atmos. Oceanic Technol.*, **8**, 118–136, https://doi.org/10.1175/1520-0426(1991)008<0118:ROMRIF>2.0.CO;2.

Xie, P., R. Joyce, S. Wu, S. H. Yoo, Y. Yarosh, F. Sun, and R. Lin, 2017: Reprocessed, bias-corrected CMORPH global high-resolution precipitation estimates from 1998. *J. Hydrometeor.*, **18**, 1617–1641, https://doi.org/10.1175/JHM-D-16-0168.1.

You, Y., N.-Y. Wang, and R. Ferraro, 2015: A prototype precipitation retrieval algorithm over land using passive microwave observations stratified by surface condition and precipitation vertical structure. *J. Geophys. Res. Atmos.*, **120**, 5295–5315, https://doi.org/10.1002/2014JD022534.